J. Fluid Mech. (2015), *vol.* 781, *pp.* 298–329. © Cambridge University Press 2015
doi:10.1017/jfm.2015.497

The intermittency boundary in stratified plane Couette flow

Enrico Deusebio[1], **C. P. Caulfield**[2,1] **and J. R. Taylor**[1,†]

[1]Department of Applied Mathematics and Theoretical Physics, University of Cambridge, Centre for Mathematical Sciences, Wilberforce Road, Cambridge CB3 0WA, UK

[2]BP Institute, University of Cambridge, Madingley Road, Cambridge CB3 0EZ, UK

(Received 20 February 2015; revised 30 June 2015; accepted 18 August 2015; first published online 18 September 2015)

We study stratified turbulence in plane Couette flow using direct numerical simulations. Two external dimensionless parameters control the dynamics, the Reynolds number $Re = Uh/\nu$ and the bulk Richardson number $Ri = g\alpha_V Th/U^2$, where U and T are half the velocity and temperature difference between the two walls respectively, h is the half channel depth, ν is the kinematic viscosity and $g\alpha_V$ is the buoyancy parameter. We focus on spatio-temporal intermittency due to stratification and we explore the boundary between fully developed turbulence and intermittent flow in the *Re*–*Ri* plane. The structures populating the intermittent flow regime show coexistence between laminar and turbulent patches, and we demonstrate that there are qualitative differences between the previously studied low-*Re* low-*Ri* intermittent regime and the high-*Re* high-*Ri* intermittent regime. At low-*Re* low-*Ri*, turbulent regions span the entire gap, whereas at high-*Re* high-*Ri*, turbulence is confined vertically with complex dynamics arising from interacting turbulent layers. Consistent with a previous investigation of Flores & Riley (*Boundary-Layer Meteorol.*, vol. 129 (2), 2010, pp. 241–259), we present evidence suggesting that intermittency in the asymptotic regime of high-*Re* Couette flows appears for $L^+ < 200$, where $L^+ = Lu_\tau/\nu$, with L being the Monin–Obukhov length scale, $L = u_\tau^3/C_\kappa q_w$, q_w the wall heat flux, C_κ the von Kármán constant and $u_\tau = \sqrt{\tau_w/\rho_0}$ the friction velocity determined from the wall shear stress τ_w, where ρ_0 is the constant background density. We also consider the mixing as quantified by various versions of the flux Richardson number Ri_f, defined as the ratio of the conversion rate from kinetic to potential energy to the turbulent kinetic energy injection rate due to shear. We investigate how laminar and turbulent regions separately contribute to the overall mixing. Remarkably, we find that although fluctuations are greatly suppressed in the laminar regions, Ri_f does not change significantly compared with its value in turbulent regions. As we observe a tight coupling between the mean temperature and velocity fields, we demonstrate that both Monin–Obukhov self-similarity theory (Monin & Obukhov, *Contrib. Geophys. Inst. Acad. Sci. USSR*, vol. 151, 1954, pp. 163–187) and the explicit algebraic model of Lazeroms *et al.* (*J. Fluid Mech.*, vol. 723, 2013, pp. 91–125) predict the mean profiles well. We thus use these models to trace out the boundary between fully developed turbulence and intermittency in the *Re*–*Ri* plane.

Key words: intermittency, stratified turbulence, turbulent flows

† Email address for correspondence: jrt51@cam.ac.uk

1. Introduction

Flows characterised by strong stable density stratification are encountered in many geophysical applications. In the atmosphere, boundary layers with strong static stability are observed in polar regions or during clear nights as a result of strong cooling at the ground (Nieuwstadt 1984; van de Wiel *et al.* 2002; Grachev *et al.* 2005). In the oceans, pycnoclines are similarly characterised by large density gradients due to variations in the temperature and salinity profiles (Taylor & Sarkar 2007). Under such strongly stratified conditions, turbulence can be virtually absent for a long period of time and then occur intermittently at other times in strong bursts (Kondo, Kanechika & Yasuda 1978).

In order to classify observations of the stable atmospheric boundary layer, Mahrt *et al.* (1998) proposed two dynamical regimes which he referred to as the 'weakly stable' regime and the 'very stable' regime. In the weakly stable regime, the stabilising effect of stratification is not strong enough to suppress turbulence and continuously turbulent states are typically observed. The resulting regime is relatively well understood, and theoretical approaches, such as the self-similarity theory of Monin–Obhukov (Monin & Obukhov 1954; Obukhov 1971), provide a satisfactory agreement with observations. On the other hand, the strongly stable regime is less well understood and more challenging to model.

Perhaps one of the most important and poorly understood issues is the characterisation of mixing processes. Although many models assume a fixed ratio between buoyancy flux and kinetic energy dissipation of approximately 0.2 (Osborn 1980; Wunsch & Ferrari 2004), there is very large uncertainty as to what the mixing efficiency is and, indeed, whether it is constant (e.g. Smyth, Moum & Caldwell 2001). Linden (1979) reported experimental observations of the mixing efficiency quantified by the flux Richardson number Ri_f, defined as the ratio of the conversion rate from kinetic to potential energy to the turbulent kinetic energy injection rate due to shear. Although a rather large spread of data was observed, Ri_f was found to increase with the bulk Richardson number, Ri, up to a maximum of $Ri_f \approx 0.2$ for $Ri \lesssim 0.1$–0.15 and decrease for larger values of Ri. As originally argued by Phillips (1972), if the buoyancy flux decreases with stratification at relatively large static stability, there is an effectively negative eddy diffusivity. As a result, small perturbations in the density profile are unstable and lead to the creation of sharp interfaces between relatively well-mixed layers, a rather striking feature observed in a number of experiments of stably stratified flows (Ruddick, McDougall & Turner 1989; Park, Whitehead & Gnanadeskian 1994; Holford & Linden 1999). Recent experiments by Oglethorpe, Caulfield & Woods (2013) have also suggested the presence of a plateau in the mixing efficiency for large stratifications, possibly connected to self-similar regimes of strongly stratified turbulence (Billant & Chomaz 2001).

More importantly, it is unclear how the mixing efficiency is influenced by the appearance of global intermittency characterising strongly stratified regimes (van de Wiel *et al.* 2002; van de Wiel, Moene & Jonker 2012) where laminar and turbulent regions coexist and mutually interact. Although strongly stratified flows are known to be highly intermittent (Rorai, Mininni & Pouquet 2014), large-scale intermittency and coexistence of laminar and turbulent dynamics may also arise in unstratified conditions at low Reynolds number, Re, due to viscous effects 'quenching' the turbulence. Coles (1965) conducted a number of Taylor–Couette flow (TCF) experiments investigating the transition from laminar finite-amplitude instabilities to turbulence. Intermittent states were observed, characterised by spiral bands of turbulence alternating with laminar regions. More recently, Prigent *et al.* (2002) also performed experiments on

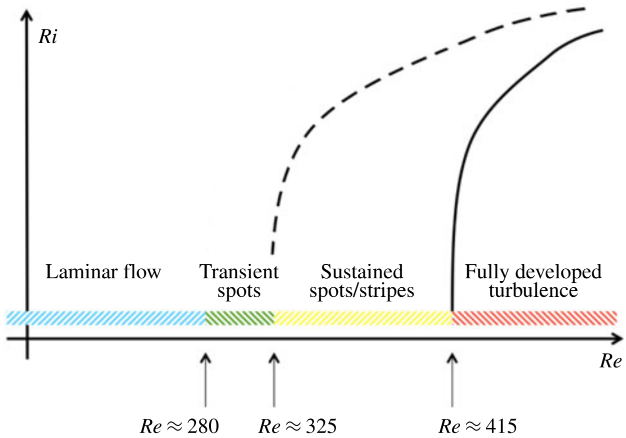

FIGURE 1. (Colour online) Sketch of the intermittency boundary (solid line) and the relaminarisation boundary (dashed line) in the *Re*–*Ri* plane of Couette flows.

more extended domains, showing the existence of similar large-scale modulations in both plane Couette flow (PCF) and TCF for $340 < Re < 415$, where $Re = Uh/\nu$ is here defined using half the velocity difference U, the half channel gap h and the kinematic viscosity of the fluid ν. The appearance of inclined bands of laminar/turbulent regions has recently been studied numerically, both in small aspect-ratio domains perpendicular to the bands (Barkley & Tuckerman 2005, 2007) and in extended domains (Duguet, Schlatter & Henningson 2010).

Similar structures have also been found at higher Re when a stabilising force other than viscosity suppresses turbulent motions. García-Villalba & del Álamo (2011) reported intermittent dynamics in stratified channel flows in the form of laminar spots surrounded by turbulent dynamics. Brethouwer, Duguet & Schlatter (2012) showed coexistence of laminar/turbulent inclined bands in spanwise rotating Couette flow and in channel flows subjected to buoyancy or magnetic forces. Ansorge & Mellado (2014) and Deusebio *et al.* (2014) found inclined turbulent/laminar stripes in stratified Ekman layers, i.e. boundary layers developing under the effect of wall-normal rotation, which indicates that turbulent patterns might be more general and not limited to TCF and PCF dynamics only.

The introduction of a stabilising force into the system, such as stratification, allows us to have an additional control parameter to study the complexity arising from the temporal and spatial intermittency of the flow. Figure 1 shows a cartoon of the phase space of stably stratified PCF where two dimensionless parameters control the dynamics, the bulk Reynolds number Re and the bulk Richardson number Ri. The two lines show the intermittency boundary (solid line) between fully developed turbulence and intermittent regimes, which crosses the zero-stratification axis at approximately $Re = 415$ (Prigent *et al.* 2002; Duguet *et al.* 2010), and the relaminarisation boundary (dashed line) to the left of which no chaotic attractor exists, crossing the zero-stratification axis at approximately $Re = 324$ (Duguet *et al.* 2010). At the present stage it is not known where the regime boundaries lie in the *Re*–*Ri* plane, and the main aim of the current investigation is to be able to identify the intermittency boundary. On the other hand, tracing the relaminarisation boundary is beyond the scope of the present study, although there have been some recent investigations of this issue focusing on the identification of minimal seeds (Eaves & Caulfield 2015) and edge states (Olvera & Kerswell 2014) in stably stratified PCF. The two boundaries are distinct and well separated at low *Re*. Nevertheless, it is unclear whether they would approach each other and possibly coalesce at higher *Re*.

The quest to trace out these boundaries is connected with the development of an understanding of the relaminarisation process and the maintenance of wall-bounded turbulence. Early approaches, such as the Miles–Howard criterion (Howard 1961; Miles 1961), related relaminarisation to either linear stability analysis of shear flows or to the balance between turbulent kinetic energy production by shear and conversion to potential energy (e.g. Armenio & Sarkar 2002). Nieuwstadt (2005) presented evidence that the relaminarisation of open-channel flows subject to strong cooling at the lower wall occurs when $h/L \approx 0.5$, where h is the half channel gap and

$$L = u_\tau^3 / C_\kappa q_w \tag{1.1}$$

is the Obukhov length scale (Monin & Obukhov 1954), with $u_\tau^2 = \rho_0 \tau_w$ being the friction velocity, $C_\kappa \approx 0.4$ the von Kármán constant, q_w the wall heat flux and τ_w the shear stress at the wall. Flores & Riley (2010) suggested, however, that the critical value of h/L may be *Re*-dependent and proposed that a criterion based on L^+ should instead be used, where $L^+ = L u_\tau / \nu$ is the Monin–Obukhov length scale normalised in wall units.

From a physical point of view, the L^+ criterion suggests that relaminarisation is inherently a near-wall process for wall-bounded flows. The importance of near-wall dynamics to sustain wall-bounded turbulence in unstratified flows has been recognised for a long time. The region close to the wall is the place where most of the turbulent kinetic energy is generated (near $y = 15\nu/u_\tau$) and fluctuations are the largest (see, for instance, Kim, Moin & Moser 1987). Hamilton, Kim & Waleffe (1995) identified a self-sustained near-wall process in which counter-rotating streamwise vortices produce high- and low-velocity streaks by advecting the mean flow. These streaks are unstable in the inviscid limit and their secondary instability leads to the formation of new streamwise vortices, hence the cycle. The importance of the so-called near-wall cycle in wall-bounded turbulent dynamics has also been emphasised by synthetic simulations in which horizontally periodic boxes were reduced until turbulence could no longer be sustained (Jiménez & Moin 1991). The spanwise extent of the minimal flow unit, i.e. the smallest box size able to allow the development of turbulent flows, was found to be of the order of the near-wall streak spacing. Jiménez & Pinelli (1999) extended this to the vertical direction by damping out turbulent fluctuations above a certain height δ and showed that turbulence can only be sustained if $\delta > 60\nu/u_\tau$.

Here, we will provide evidence that suggests that the onset of intermittency in strongly stratified PCF is indeed connected with the suppression of the near-wall cycle and that the criterion proposed by Flores & Riley (2010) based on L^+ can capture the onset of intermittent dynamics in the asymptotic regime of high-*Re* stably stratified PCF. When the flow is indeed turbulent, we also investigate the efficiency of mixing using several definitions of the flux Richardson number Ri_f. When Ri_f is defined in terms of global quantities describing the energy input by the wall forcing and the buoyancy flux through the boundaries, we find that Ri_f increases linearly with Ri, due to the fact that the mean velocity and density profiles are related by $q_w/T \approx \tau_w/U$ in the canonical geometry of PCF. We have also found that appropriate measures of Ri_f take close to the same values in both laminar and turbulent regions of the flow when it is spatially intermittent. Although there has been recent interesting work considering in detail the most appropriate measure of mixing efficiency (see, for example, Karimpour & Venayagamoorthy 2015; Salehipour & Peltier 2015), since we are focused on intermittency, we believe that slight modifications of the classical definition of the flux Richardson number adequately capture the (interestingly weak) effect of intermittency on the 'efficiency' of mixing.

Consistent with this observation, we confirm that Monin–Obukhov theory is able to provide a reasonable description of the velocity and temperature mean profiles, comparable to more sophisticated models such as the explicit algebraic model (EAM) developed by Lazeroms *et al.* (2013). We then use these models to predict the intermittency boundary in the *Re*–*Ri* phase space separating the intermittent and fully developed turbulent regimes, and demonstrate good agreement between these predictions and the results of our numerical simulations.

The paper is organised as follows: § 2 gives a summary of the numerical code and an overview of the simulations; § 3 presents mean global quantities and turbulent fluctuations; § 4 describes phenomenologically the intermittent regimes of PCF; § 5 investigates the efficiency of mixing considering different definitions of Ri_f; in § 6 we develop an analytical model based on Monin–Obukhov self-similarity theory and an EAM to predict the boundary between fully turbulent and intermittent dynamics and we compare this prediction with our simulations; finally, § 7 provides conclusions and final remarks.

2. Numerical set-up

We consider a temperature-stratified system described by the Navier–Stokes equations under the Boussinesq approximation where density variations are related to temperature variations via a linear equation of state, i.e.

$$\frac{\partial \boldsymbol{u}}{\partial t} + \boldsymbol{u}\boldsymbol{\cdot}\boldsymbol{\nabla}\boldsymbol{u} = -\frac{\boldsymbol{\nabla} p}{\rho_0} + \nu\nabla^2\boldsymbol{u} - g\alpha_V T\boldsymbol{e}_y, \tag{2.1a}$$

$$\frac{\partial T}{\partial t} + \boldsymbol{u}\boldsymbol{\cdot}\boldsymbol{\nabla}T = \kappa\nabla^2 T, \tag{2.1b}$$

$$\boldsymbol{\nabla}\boldsymbol{\cdot}\boldsymbol{u} = 0. \tag{2.1c}$$

Here, $\boldsymbol{u} = (u, v, w)$ is the velocity vector in the reference system (x, y, z) with x and z being the horizontal coordinates and y the vertical coordinate, p is the pressure, ρ_0 is the background reference density, T is the temperature and $g\,\alpha_V$ is the 'buoyancy parameter', with α_V being the thermal expansion coefficient and g the gravity. The molecular kinematic viscosity ν and thermal diffusivity κ are assumed to be constant.

Periodic boundary conditions are imposed in the x and z directions. In the vertical direction, the velocity and the temperature satisfy Dirichlet boundary conditions at the two counter-moving walls, i.e.

$$u = -U, \quad v = 0, \quad w = 0, \quad T = -T_r \tag{2.2a–d}$$

at $y = -h$ and

$$u = U, \quad v = 0, \quad w = 0, \quad T = T_r \tag{2.3a–d}$$

at $y = h$. When not otherwise stated, in the following we will always refer to the dimensionless counterparts of the quantities which have been normalised using U as a reference velocity, T_r as a reference temperature and h as a reference length. The dynamics can be described in terms of three dimensionless parameters: the bulk Reynolds number Re,

$$Re = \frac{Uh}{\nu}, \tag{2.4}$$

the bulk Richardson number,

$$Ri = \frac{g\alpha_V T_r h}{U^2}, \tag{2.5}$$

and the Prandtl number,

$$Pr = \frac{\nu}{\kappa}. \tag{2.6}$$

Here, we consider $Pr = 0.7$ as a model of temperature stratification in air. It is important to note that the wall shear stress

$$\tau_w = \nu \left. \frac{\partial u}{\partial y} \right|_{y=\pm 1} \tag{2.7}$$

and heat flux

$$q_w = \kappa \left. \frac{\partial T}{\partial y} \right|_{y=\pm 1} \tag{2.8}$$

are not prescribed but naturally arise from the dynamics. As a consequence, the friction Reynolds number, defined using the friction velocity $u_\tau = \sqrt{\tau_w/\rho_0}$,

$$Re_\tau = \frac{u_\tau h}{\nu} \quad \text{with} \ \rho_0 u_\tau^2 = \tau_w, \tag{2.9}$$

which quantifies the ratio between the largest scales $\sim h$ and the smallest scales $\sim \nu/u_\tau$, and the Nusselt number,

$$Nu = \frac{q_w h}{\kappa T_r}, \tag{2.10}$$

used to estimate the heat transfer are unknown *a priori* and are to be considered as output parameters.

Equations (2.1) together with the boundary conditions (2.2)–(2.3) have been discretised using Fourier modes in the two horizontal directions and second-order finite differences in the vertical direction. Time stepping was achieved by means of a low-storage third-order Runge–Kutta method for the nonlinear terms and a semi-implicit Crank–Nicolson method for updating viscous and diffusive terms. Nonlinear terms were evaluated in physical space and a 2/3 dealiasing rule was applied when transforming back to Fourier space. Variable time steps based on a Courant–Friedrichs–Lewy (CFL) number equal to 0.5 were employed. For further details on the numerical scheme we refer the interested reader to Taylor (2008) and Bewley (2010). In order to carry out high-resolution numerical simulations, the code was parallelised by using a 2D domain decomposition and parallel transpose operations. Good scalability was observed up to a few thousand processors.

Figure 2 shows a summary in the *Re*–*Ri* plane of the simulations which did not relaminarise within the used time window (in all the cases larger than 1000 h/U, corresponding to 10–20h/u_τ). The simulations span more than two orders of magnitude in *Re* and values of *Ri* that range between 0 and 0.175. Similarly to the simulations of García-Villalba, Azagra & Uhlmann (2011), in runs 1 to 16 in table 1 we consider sets of *Re*–*Ri* values that keep Re_τ approximately constant. Simulations were initialised by fixing *Ri* and adjusting *Re* every 100 time steps such that the target value of Re_τ was achieved. This allowed us to find an estimate of *Re* which was then held fixed. The reason for fixing Re_τ rather than *Re* is twofold: first,

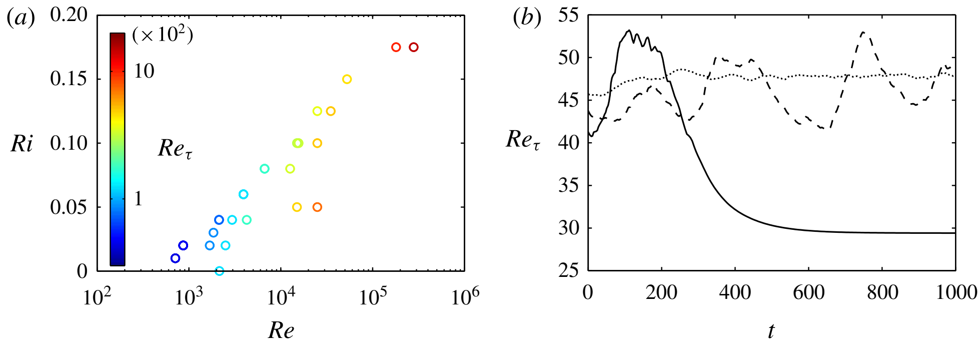

FIGURE 2. (a) Summary of the simulations (listed in table 1), in the Re–Ri plane. Colours represent the magnitude of the Re_τ, ranging from 40 (blue) to 1500 (red); (b) Re_τ for the same set of parameters of simulation 2 for different box sizes: ——, $(L_x, L_z) = (8\pi, 4\pi)$; - - - -, $(L_x, L_z) = (16\pi, 8\pi)$; · · · · · ·, $(L_x, L_z) = (32\pi, 16\pi)$.

Run	Re	Re_τ	Ri	L_x	L_z	N_x	N_y	N_z	L^+	γ
1	710	45	0.01	16π	8π	512	65	512	578	0.87
2	865	47	0.02	64π	32π	1024	65	1024	256	0.64
3	1 685	90	0.02	4π	2π	128	97	128	492	1.00
4	1 850	90	0.03	4π	2π	192	97	192	297	0.88
5	2 130	85	0.04	32π	16π	1024	97	1024	170	0.50
6	2 150	127	0.0	4π	2π	192	129	192	Inf	1.00
7	2 950	128	0.04	4π	2π	192	129	192	287	0.99
8	3 925	130	0.06	16π	8π	768	129	768	148	0.82
9	4 250	181	0.04	4π	2π	256	129	256	395	1.00
10	6 666	182	0.08	8π	4π	256	129	256	128	0.83
11	12 650	349	0.08	4π	2π	512	161	512	249	1.00
12	15 600	335	0.1	4π	2π	512	193	512	152	0.91
13	35 000	520	0.125	4π	2π	768	289	768	134	0.79
14	52 630	469	0.15	4π	2π	768	289	768	59	0.28
15	180 000	1043	0.175	4.0	2.0	512	385	512	75	0.41
16	280 000	1578	0.175	2.66	1.33	512	513	512	117	0.70
A	15 000	497	0.05	4π	2π	768	257	768	666	1.00
B	15 000	318	0.1	4π	2π	512	193	512	142	0.85
C	25 000	764	0.05	4π	2π	768	385	768	930	1.00
D	25 000	520	0.1	4π	2π	768	257	768	227	0.99
E	25 000	377	0.125	4π	2π	640	225	640	96	0.61

TABLE 1. Summary of the characteristics of the simulations.

it is Re_τ that imposes the requirements for a fully resolved simulation; second, it is Re_τ that defines the ratio between largest and smallest scales.

Eight values of Re_τ were chosen, ranging from 45 (close to the value of unstratified relaminarisation) up to 1500. Two sets of simulations at constant $Re = 1.5 \times 10^4$ and $Re = 2.5 \times 10^4$ were also run (runs from A to E in table 1). Figure 2(a) shows Re_τ by the colour of the open circles marking the Re–Ri plane. As is evident, constant-Re_τ contours are sloped lines at increasing Re and increasing Ri. We increase Ri until (partially) turbulent states cannot be sustained and full relaminarisation is achieved. As shown in figure 2(*a*), relaminarisation occurs at larger Ri as Re_τ (and Re) increases.

Table 1 lists the numerical parameters of the simulations. Here, N_x, N_y and N_z represent the number of points in physical space along the streamwise, wall-normal and spanwise directions respectively; γ represents the fraction of the flow considered to be turbulent, and its actual definition will be further discussed in § 4.2; L^+ represents the ratio between the Monin–Obukhov length scale (Obukhov 1971; Monin & Obukhov 1954),

$$L = \frac{u_\tau^3}{C_\kappa q_w}, \tag{2.11}$$

and the wall viscous length scale, $l = \nu/u_\tau$, i.e.

$$L^+ = \frac{L}{l} = \frac{u_\tau L}{\nu}, \tag{2.12}$$

where C_κ in (2.11) is the von Kármán coefficient, i.e. $C_\kappa \approx 0.4$. From a physical point of view, the Monin–Obukhov length scale L is a measure of the distance from the wall at which buoyancy forces affect the dynamics, where injection of turbulent kinetic energy and conversion to potential energy are of similar magnitude, whereas l is the relevant length scale for near-wall dynamics. The results at $Re_\tau = 130$ and $Re_\tau \approx 540$ were found to be in agreement with the simulations of García-Villalba *et al.* (2011), thus providing a validation of the numerical tool used in the present investigation. When feasible, several box sizes were considered in order to check the convergence as well as the sensitivity of our results with respect to the box dimensions. Table 1 only summarises the simulations with the largest horizontal extents. For the lowest friction Reynolds numbers, we consider computational domains as large as $L_x = 200h$ and $L_z = 100h$, producing sustained inclined striped patterns similar to those observed by Barkley & Tuckerman (2005), Brethouwer *et al.* (2012) and Duguet & Schlatter (2013).

Following general guidelines for direct numerical simulations of wall-bounded turbulence (Moin & Mahesh 1998), we adjust the grid spacing such that $\Delta x^+ \approx 8$, $\Delta z^+ \approx 4$ and $y_{10}^+ < 10$, where y_{10} is the tenth point from the wall and the $+$ superscript represents quantities normalised using viscous scaling, i.e. using l for length scales and u_τ for velocities. As Re_τ increases, the grid spacing required to resolve the smallest turbulent length scales decreases, making it necessary to reduce the size of the computational domain in order to reduce the computational cost. It is important to appreciate that our results may be dependent on the size of the computational domain and that the dimensions considered in some simulations (e.g. 15 and 16 in table 1) may well be close to marginal, according to the guidelines provided by Flores & Jiménez (2010). However, as we will discuss below, these simulations allow us to gain some insight into the intermittent dynamics and an estimate of the intermittency at high Re despite the reduced dimensions. The smallest computational domain considered (at $Re_\tau = 1500$) has $L_x = 2.67h$ and $L_z = 1.33h$, corresponding in viscous units to $L_x^+ \approx 4000$ and $L_z^+ \approx 2000$.

The size of the computational domain affects the results significantly only when coexistence between laminar and turbulent patches arises. Figure 2(*b*) shows the time evolution of Re_τ for a simulation at $Re = 865$ and $Ri = 0.02$. For a small computational domain size, turbulence cannot be sustained and full relaminarisation is observed. When the computational domain is marginal, the flow stays turbulent, but it exhibits temporal intermittency with large fluctuations (approximately 5–10 %)

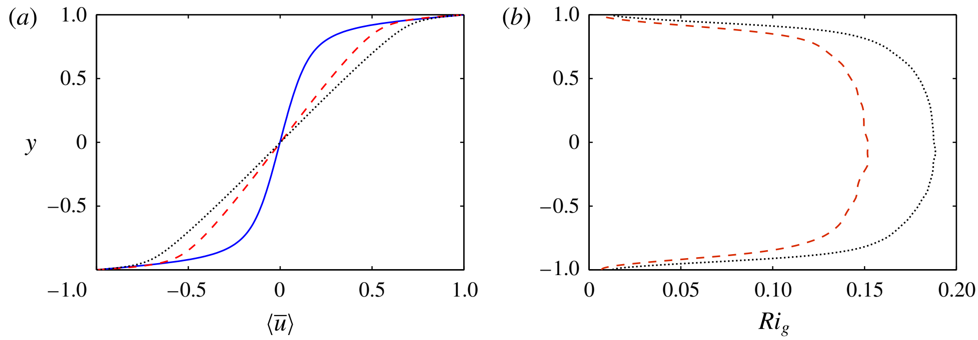

FIGURE 3. (Colour online) Vertical profiles of (*a*) $\langle \overline{u} \rangle$ and (*b*) Ri_g: simulation 6 (——), simulation 11 (- - - -) and simulation 13 (· · · · · ·).

of Re_τ. As the size of the computational domain increases, temporal intermittency is suppressed and replaced by spatial intermittency. Interestingly, we find that time averages of global quantities (such as Re_τ, Nu and the turbulent fraction γ) vary only by a few per cent with the size of the computational domain as long as the flow stays at least partially turbulent. In particular, we find that for the case in figure 2(*b*) (simulation 2) the time-averaged turbulent fraction γ in various domains varies between 60 % and 65 %. However, we find that the size of the computational domain significantly affects the qualitative patterns of the laminar/turbulent patches in the intermittent regime. Turbulent and laminar patches tend to be aligned in the streamwise direction in small computational domains, whereas as the domain size increases, inclined laminar/turbulent bands similar to the findings of Duguet *et al.* (2010) are found.

3. One-point statistics

Figure 3(*a*) shows the mean streamwise velocity profiles $\langle \overline{u} \rangle$ for three different simulations at increasing Re and Ri. In the following, we will use the overbar $\bar{\cdot}$ to denote a horizontal average and the brackets $\langle \cdot \rangle$ to denote the time average extending over the entire simulation. As Ri increases, a constant-shear region appears in the core of the flow. It is worth noting that this region is still turbulent and the observed linear profile results from stratified turbulent dynamics rather than from a purely laminar flow. The development of a constant-shear region can be explained by a suppression of the local turbulent length scale by stratification. If the interior flow is independent of the distance from the walls, the turbulence, and hence the shear, is only determined by local properties (momentum and buoyancy fluxes) which are constant along y. It should be noted, however, that since the wall stress provides the driving force for turbulence in PCF, the turbulence remains dependent on the wall stress. As Re increases, the constant-shear region extends closer to the wall. Gradients at the wall do not steepen extensively because of the balancing effect of stratification which causes Re_τ to increase from 130 to 520 in spite of the much larger change in Re, from 2150 to 35 000.

The density profiles show very similar behaviour to the velocity, which is expected due to the fact that the Pr is close to unity, $Pr = 0.7$. Figure 3(*b*) shows the time-

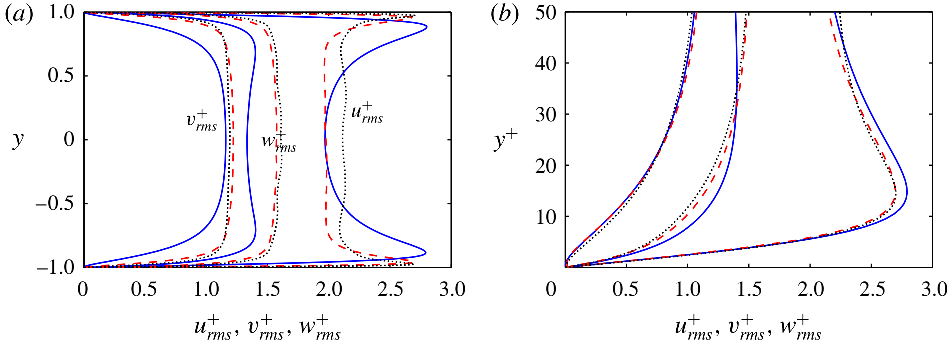

FIGURE 4. (Colour online) Velocity fluctuations: (*a*) across the channel and (*b*) blow-up near to the wall. The line types are as in figure 3.

averaged gradient Richardson number,

$$Ri_g(y) = Ri \frac{\left\langle \dfrac{\partial \overline{T}}{\partial y} \right\rangle}{\left\langle \left(\dfrac{\partial \overline{u}}{\partial y} \right)^2 \right\rangle}. \tag{3.1}$$

The gradient Richardson number, as defined in (3.1), is minimum at the wall and increases towards the centre of the channel. Using the background method (Doering & Constantin 1992), Tang, Caulfield & Kerswell (2009) identified optimal profiles that maximise buoyancy flux in stratified PCF subject only to global energetic balances and a constraint on the horizontal momentum, and found non-monotonic profiles of Ri_g exhibiting a local maximum close to the walls. The Ri_g profiles in figure 3(*b*) are not in agreement with such a prediction, suggesting that the constraints imposed by Tang *et al.* (2009) are far too weak and neglect the importance of (weakly stratified) near-wall dynamics crucial to sustain turbulence in PCF.

We find that the broad plateau developing in the core of the channel increases with Ri (figure 3*b*) and saturates in amplitude for large values smaller than 0.25, i.e. the limiting threshold for linear normal-mode stability of inviscid stably stratified shear flows. Figure 4 shows the different components of the turbulent velocity fluctuations. As shown in panel (*b*), the dynamics close to the wall generally retains viscous scalings: the location of the near-wall peak of u_{rms} in wall units is not significantly affected by changes in Re and Ri, although its intensity slightly decreases as Re and Ri increase. The intensity of streamwise fluctuations in the centre of the channel increases as the stratification (and the shear) in the core region increases.

Figure 5 shows the turbulent shear stress scaled by u_τ^2. The decrease of the magnitude of the plateau with increasing stratification indicates that a non-negligible part of the momentum (up to 10 % for the highest Ri) is transferred by molecular diffusion. Since – as we will argue below – the slopes of the mean velocity and temperature profiles are set by the stratification, at fixed Ri we would expect that $\langle \overline{u'v'} \rangle / u_\tau^2$ approaches unity as $Re \to \infty$. The turbulent heat flux (not shown) also displays very similar behaviour to the turbulent momentum flux, i.e. a constant plateau in the central region with values that asymptotically approach q_w, as defined in (2.8), as the Péclet number $Pe = Re\,Pr \to \infty$.

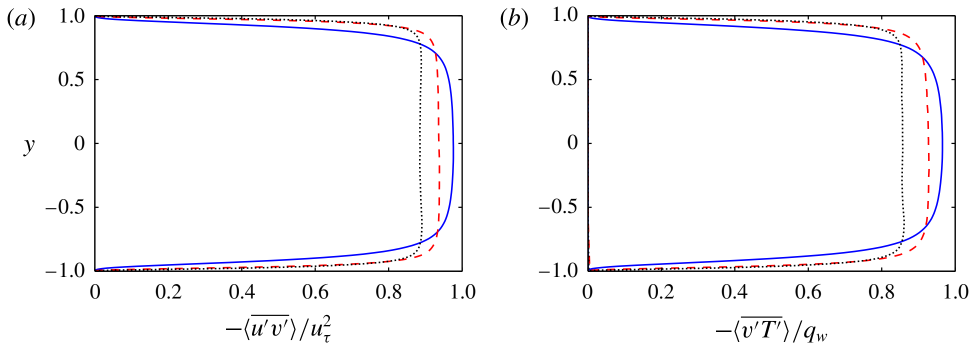

FIGURE 5. (Colour online) (*a*) Turbulent shear stress $-\langle\overline{u'v'}\rangle$, normalised by the friction velocity, u_τ^2. (*b*) Turbulent heat flux $-\langle\overline{v'T'}\rangle$, normalised by the wall heat flux, q_w. The lines are as in figure 3.

4. Intermittent dynamics

4.1. *Phenomenology of intermittency at large and low Re*

In figure 6, the streamwise velocity in a horizontal plane close to the upper wall, $y = 0.95$, is shown for three weakly intermittent simulations. The value of Re_τ increases from (*a*) to (*c*), corresponding to $Re_\tau = 130$, 180 and 520, simulations 8, 10 and 13 respectively. In all three cases, laminar patches appear in the flow, similar to those observed by García-Villalba *et al.* (2011) in stratified channel flows. It should be noted that in the three cases the dimension of the box varies considerably and the laminar patches at low Re_τ are significantly larger. Nevertheless, the three flows exhibit similar dynamics with laminar patches cyclically appearing and disappearing in the flow with time scales of the order of hundreds of convective time units. For these simulations, spatially averaged quantities show small fluctuations in time, suggesting that the chosen box sizes are suitable to study the intermittent dynamics. The degree of stratification in these cases is not strong enough to lead to the generation of sustained and steady inclined laminar/turbulent bands as observed by Brethouwer *et al.* (2012) and Deusebio *et al.* (2014). As *Ri* increases, the extent of the laminar regions increases and the dynamics becomes increasingly more intermittent in time. Figure 7(*a*) shows a snapshot of the streamwise velocity close to the upper wall, at $y = 0.95$, for simulation 14. There is only one band of turbulence spanning the entire streamwise extent, and this band is surrounded by laminar flow. As is apparent from the typical values of the streamwise velocity (the same colour bar is used in figures 6*c* and 7*a*), the streamwise velocity is substantially closer to its laminar value at $y = 0.95$ for simulation 14 than for the more vigorously turbulent simulation 13. In this simulation, Re_τ varies considerably in time, ranging between 380 and 540, which suggests that the size of the computational domain is only marginally large enough to accommodate sustained intermittent dynamics. The topology found in figure 7 was similarly observed in simulations 15 and 16, confirming that also in these cases the computational domains were close to marginal.

We only observe bands similar to those observed by Brethouwer *et al.* (2012) at low $Re_\tau < 100$, for which very large computational domains could be used. In smaller computational domains, the spatial intermittency is replaced by temporal intermittency and the turbulent bands align in the streamwise direction. However, the fact that at $Re_\tau = 540$ we find streamwise stripes of turbulence similar to those found in low-*Re*

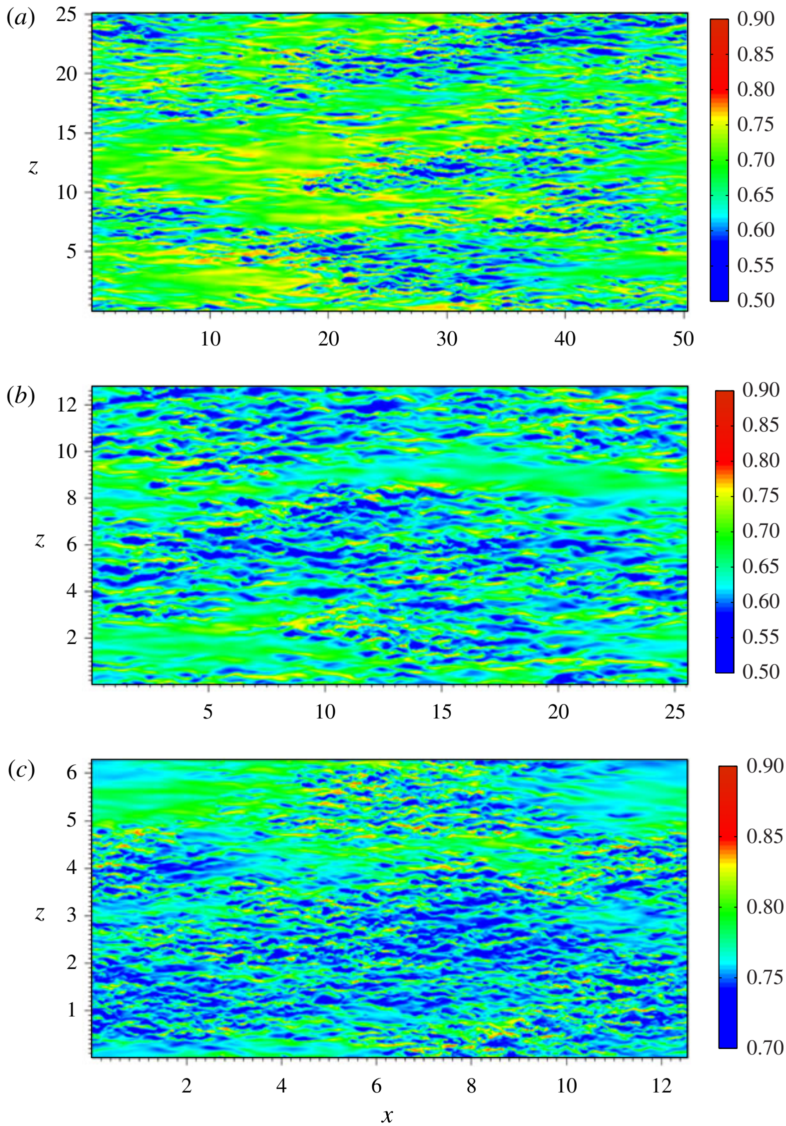

FIGURE 6. Streamwise velocity in a horizontal plane close to the upper wall, at $y=0.95$. It should be noted that the full domain is shown in each of the three cases, which vary in size. (*a*) Simulation 8; (*b*) simulation 10; (*c*) simulation 13.

small-domain simulations suggests that inclined bands might be observed at higher *Re* if larger computational domains were employed.

At low *Re*, the laminar regions extend over the entire channel depth. However, we find that the vertical structure of the laminar/turbulent regions is inherently different for simulations at low and high *Re*. As *Ri* increases, laminar regions appearing at higher *Re* become more confined to the walls. Brethouwer *et al.* (2012) found that in stratified channel flows partial relaminarisation occurs at the walls, whereas the dynamics in the interior remains highly turbulent, without any dominant presence of large-scale structures. In figure 7(*b*) the enstrophy (a useful and simple proxy

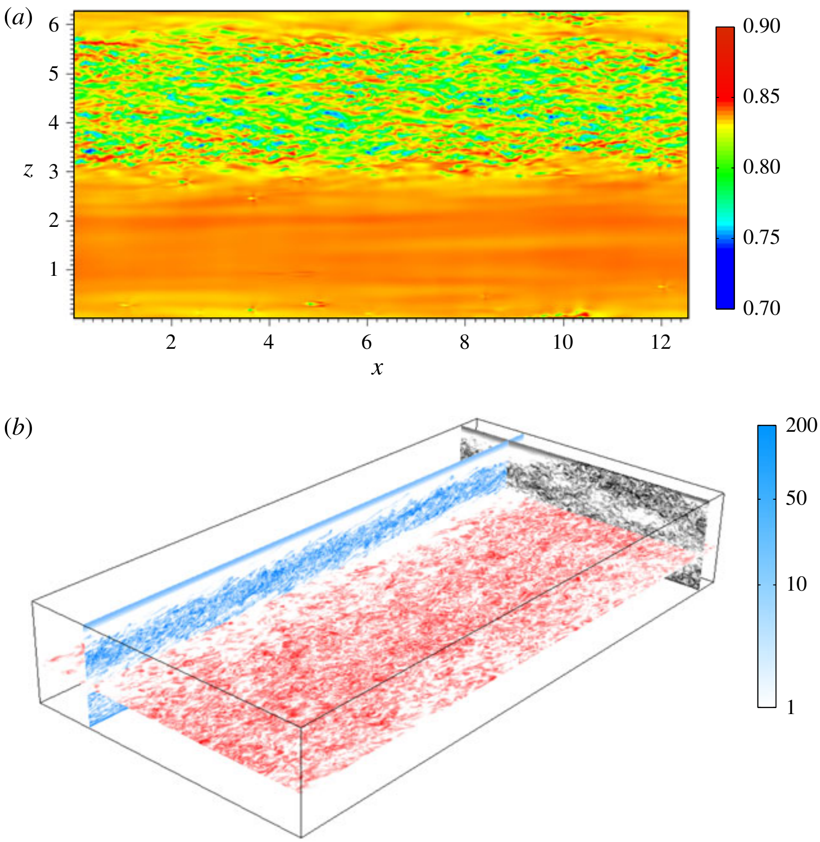

FIGURE 7. Flow field for a highly intermittent simulation (simulation 14). The entire domain is shown in both panels. (*a*) Streamwise velocity in a horizontal plane close to the upper wall, at $y = 0.95$. The full domain is shown and colours range from blue (low values) to red (high values), using the same colour bar as figure 6(*c*). (*b*) Three-dimensional view of the enstrophy in three planes normal to the Cartesian axes: x-normal at $x = 12$ (black), y-normal at $y = -0.2$ (red) and z-normal at $z = 1$ (blue). The scale logarithmically ranges from 1 U^2/h^2 to 200 U^2/h^2 and it is the same in all of the plots. Colours are used only to highlight which plane the contours belong to.

for turbulence) in planes normal to the three Cartesian axis is shown for simulation 14. The contours projected onto the three Cartesian planes are coloured differently (although with the same intensity scale). The z-normal plane clearly shows the presence of two turbulent layers separated by a quieter laminar region close to the channel mid-plane. This quieter region is confined horizontally and it is bordered in the spanwise direction by a turbulent patch which originates from the bending of the upper vertically confined turbulent layer, as shown by the x-normal plane. Figure 7(*b*) highlights a rich dynamical picture in which intermittency at the wall connects to intermittent dynamics in the centre of the channel, with streamwise turbulent layers bending and mutually interacting. The dynamical transition between the turbulent bands (filling the entire channel gap) observed at low *Re* and the layering structure in figure 7(*b*) is gradual. The bands moderately develop a spanwise inclination which leads to an inhomogeneity in the vertical direction.

It is unclear whether the absence of intermittent dynamics in the interior as observed by Brethouwer *et al.* (2012) is due to a weaker stratification or to a difference of flow configuration with respect to our simulations. It is nevertheless worth noting that in PCF intermittency at the wall significantly affects the overall dynamics. From an energetic point of view, PCF is forced by shear stresses at the upper and lower walls, and the dynamics in the interior adjusts in order to carry the momentum flux resulting from the near-wall dynamics. Full or partial relaminarisation leads to a significant drop in the magnitude of the wall shear stress τ_w, thus also strongly affecting the dynamics in the interior. The influence of the partial relaminarisation at the walls might therefore be significantly stronger than in other flow configurations where the driving force is not affected by relaminarisation, such as the channel flows considered by Brethouwer *et al.* (2012) driven by a constant pressure gradient or the throttling method used by Chung & Matheou (2012) in stably stratified homogeneous turbulence.

4.2. *Quantifying intermittency*

One of our main aims here is to describe the intermittent regime arising due to a stable stratification. In order to quantify the degree of intermittency, an objective metric based on the identification of laminar and turbulent regions is needed. Several choices are possible, including evaluation of shear stress, vertical velocity (Brethouwer *et al.* 2012) and vorticity (Corrsin & Kistler 1955; Pope 2000).

We base our criterion on the wall enstrophy,

$$\eta_{\pm}(x, z, t) = \left(\frac{\partial u}{\partial y}\right)^2 + \left(\frac{\partial w}{\partial y}\right)^2 \quad \text{at } y = \pm 1, \tag{4.1}$$

and identify the turbulent fraction γ using moments of the distribution of $\eta_{\pm}$ as discussed below. We are motivated to use the wall enstrophy by two considerations. First, as observed by Brethouwer *et al.* (2012), at large Re when intermittent dynamics appears laminar patches are generally confined close to the walls. Second, as discussed in § 4.1, because the driving force is applied at the solid walls, near-wall dynamics plays an important role in maintaining turbulence in PCF. In order to identify γ, we consider the horizontal spatial fluctuation of $\eta_{\pm}$ at the wall,

$$\eta_{\pm,mbf} = \sqrt{\frac{1}{A}\int_{x^+,z^+} \eta_{\pm}^2 \,\mathrm{d}x^+\,\mathrm{d}z^+ - \left[\frac{1}{A}\int_{x^+,z^+} \eta_{\pm}\,\mathrm{d}x^+\,\mathrm{d}z^+\right]^2}, \tag{4.2}$$

over subdomains corresponding to a minimal flow unit (Jiménez & Moin 1991), specifically $\Delta x^+ \approx 200$ and $\Delta z^+ \approx 100$, with $A = \Delta x^+ \Delta z^+$ being the subdomain area. The subscript *mbf* in (4.2) stands for minimal box fluctuation. Although here we use $\eta_{\pm}$ as a proxy in (4.2), alternative quantities could also be used, such as velocity, temperature or turbulent stresses. When the flow is laminar, the wall enstrophy $\eta_{\pm}$ is nearly homogeneous within the subdomains and small values of (4.2) are to be expected. On the other hand, in turbulent regions the streaky patterns associated with the near-wall dynamics lead to significantly larger fluctuations. This measure is similar to the measure used by Deusebio *et al.* (2014), although here there is a greater focus on identifying an appropriate threshold between laminar and turbulent regions. Figure 8(*a*) shows some examples of the probability density function (p.d.f.) of (4.2). The cases are characterised by different levels of intermittency: fully developed turbulence has a p.d.f. resembling a log-normal shape (the x-axis has a logarithmic

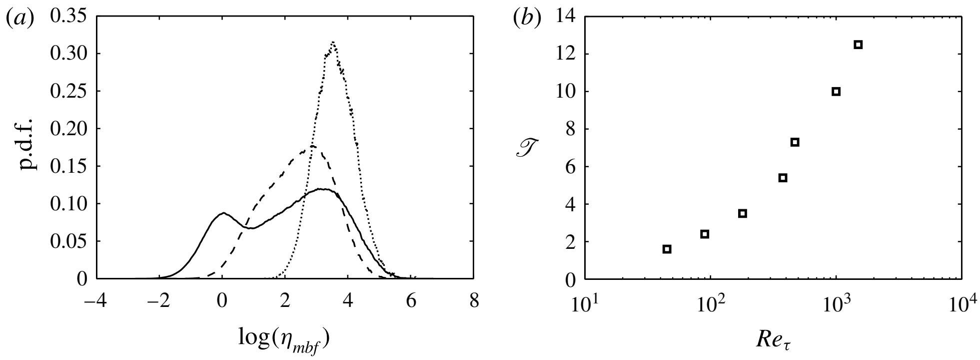

FIGURE 8. (*a*) Examples of p.d.f.s of small-box fluctuations of $\eta_\pm$ for a typical fully turbulent simulation (······, simulation 9), weakly intermittent simulation (- - - -, simulation 10) and strongly intermittent simulation (——, simulation E). (*b*) Variation of $\mathscr{T}$ with Re_τ.

scale) with a single well-identified peak (Örlü & Schlatter 2011). As intermittent dynamics occurs in the flow, the p.d.f. skews towards the left part of the plot and, in sufficiently strongly intermittent cases, a double peak appears. The double-peak shape also allows us to identify a threshold $\mathscr{T}$ separating turbulent and laminar regions as the local minimum between the two peaks of the p.d.f. We identify laminar flow at the upper or lower wall as the region for which $\eta_{\pm,mbf} < \mathscr{T}$ and turbulent flow as the region for which $\eta_{\pm,mbf} > \mathscr{T}$. In general, the threshold $\mathscr{T}$ may depend on Re_τ and we have determined its Re_τ dependence (shown in figure 8*b*) by considering the most intermittent simulations at several values of Re_τ. Although the value of the threshold increases with Re_τ, it does not vary as strongly as the range spanned by the p.d.f., which in intermittent cases extends over several orders of magnitude. In the following we will consider the intermittency factor γ for all of the simulations in table 1 by taking the average of the fraction of the upper and lower wall area for which $\eta_\pm > \mathscr{T}$ respectively. Typically, these two values are close. The algorithm described above was applied to single flow fields and results were averaged over at least 30 different sample times approximately equally spaced during the simulation.

Although we mostly focus on the near-wall value of γ, in order to study the mixing properties of laminar and turbulent regions separately (as discussed in § 5), we have further extended the algorithm to horizontal planes away from the wall using the total enstrophy in place of its wall value $\eta_\pm$. To account for the vertical inhomogeneity, we have adjusted the value of the threshold $\mathscr{T}$ based on the local turbulent kinetic energy dissipation, $\varepsilon_K = Re^{-1}\langle\overline{\partial u_i'/\partial x_j \partial u_i'/\partial x_j}\rangle$, as

$$\mathscr{T}_s(y) = \frac{\mathscr{T}}{\varepsilon_{K,\pm 1}}\varepsilon_K(y), \tag{4.3}$$

where the ± 1 subscript denotes upper and lower wall values respectively. Using the threshold $\mathscr{T}_s$, we define the vertically varying intermittency factor γ_s as the ratio of the turbulent area to the total area for each horizontal plane. Figure 9 shows an example of the identification of laminar/turbulent regions for the flow field shown in figure 6(*c*). Laminar and turbulent boundaries are well estimated, both close to

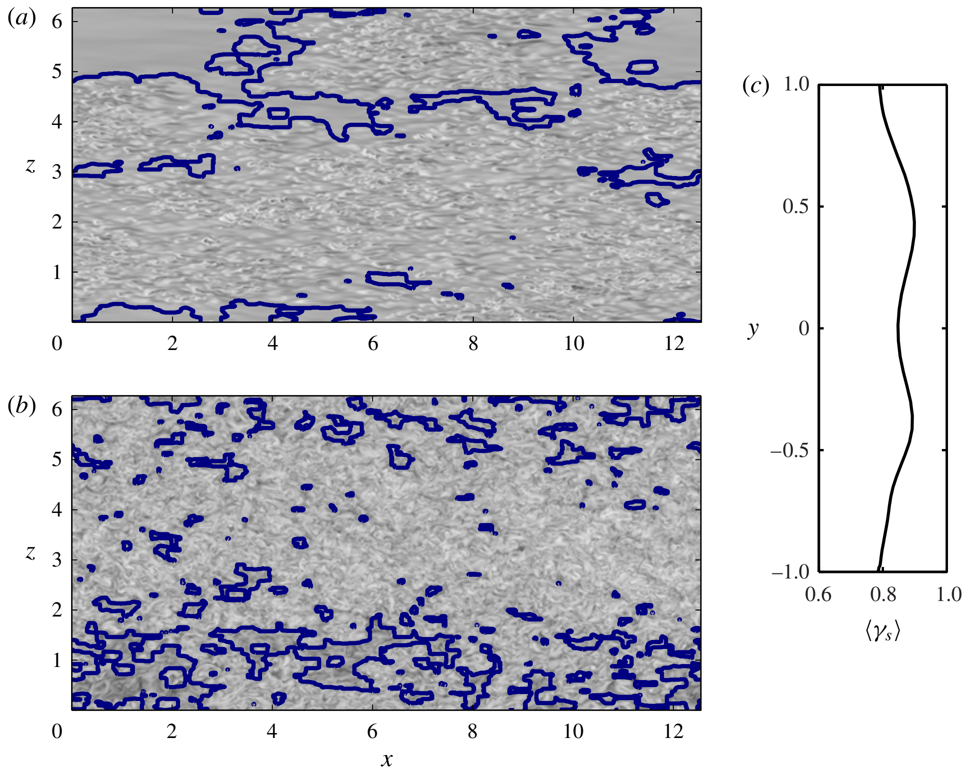

FIGURE 9. (Colour online) Identification of laminar and turbulent regions using the automatic algorithm outlined in § 4.2 for a snapshot of simulation 13 at (*a*) $y = 0.95$ and (*b*) $y = 0$. The thick line represents the boundary between laminar and turbulent regions which has been overlaid on the enstrophy field for reference. The flow corresponds to the same time instant as the flow depicted in figure 6(*c*) (simulation 13). (*c*) Wall-normal evolution of the intermittency factor γ_s (averaged over roughly 30 snapshots).

the wall, as shown in figure 9(*a*) and in the centre of the channel, as shown in figure 9(*b*). The average value of γ_s using roughly 30 flow fields (shown in figure 9*c*) slightly varies in the vertical direction, with somewhat smaller values close to the wall, where an overall intermittency factor of 82 % is found. This is consistent with the observation of Brethouwer *et al.* (2012), who found laminar patches to be mostly confined at the wall. That the smallest value of γ_s generally corresponds to the wall value γ also supports our conjecture that the relaminarisation process in stratified PCF originates in the near-wall region.

4.3. *Scaling of intermittent dynamics*

As discussed in the introduction, the most appropriate indicator for the onset of intermittent dynamics is still an open issue and several criteria have been proposed. The general disagreement on the relevant quantity generally reflects the fact that it is not yet clear which physical process governs relaminarisation and how to model it. The Miles–Howard criterion (Howard 1961; Miles 1961), based on linear stability analysis of a stratified shear layer, is sometimes invoked to explain the suppression of turbulence, although there is now a growing consensus that turbulence

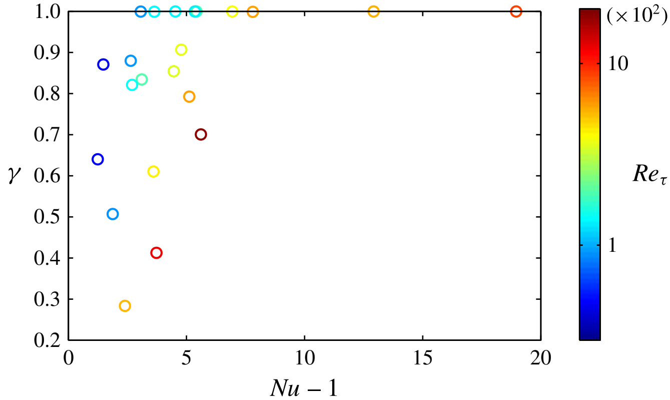

FIGURE 10. A plot of γ versus $Nu - 1$ for the entire set of simulations listed in table 1. The colour code represents Re_τ, ranging from 40 (blue) to 1500 (red).

may still be observed even when $Ri_g > 1/4$ (see, for example, Zilitinkevich *et al.* 2008). As shown in figure 3(*b*), Ri_g attains small values at the wall and increases towards the centreline, the location at which higher values are generally found. The maximum values of Ri_g before the onset of intermittency and relaminarisation show an approximate dependence with bulk Ri, and no single value describes the appearance of intermittency. Besides, intermittency is observed at the wall where Ri_g is small, $Ri_g < 1/4$.

García-Villalba & del Álamo (2011) used the Nusselt number Nu, as defined in (2.10), as a criterion to identify the appearance of intermittency in stratified channel flows, arguing that relaminarisation occurs as Nu approaches unity. This criterion is tested in figure 10, where γ is plotted against $Nu - 1$. Although as intermittency increases the data generally tend to lower values of Nu, a general scaling cannot be observed and the data show a large scatter with Re_τ.

As noted in the introduction, another criterion was proposed by Flores & Riley (2010), who hypothesised that relaminarisation is observed when $L^+ \approx 100$, thus suggesting that relaminarisation is a near-wall process since L^+ is a criterion only based on inner-scaling quantities. We test this hypothesis in figure 11, where the turbulent fraction γ is plotted versus L^+ for all of the simulations listed in table 1. We note that, apart from the two lowest values of Re_τ (plotted with the four darkest blue points in the plot), the data collapse onto a single curve, unlike the data shown in figure 10. This is quite remarkable given the Re_τ span considered in the study, which covers more than one order of magnitude. The failure to collapse the two lowest values of Re_τ is also not surprising as the L^+ criterion is expected to apply only when the onset of intermittency is determined by the imposed stratification as opposed to by viscous effects. For smaller Re values, viscosity becomes crucial and leads to a viscosity-driven intermittency, which in the unstratified limit occurs when $Re \approx 325$, corresponding to $Re_\tau \approx 35$. Nevertheless, the asymptotic regime in which intermittency dynamics is buoyancy-driven and the intermittency factor γ becomes independent of Re is already reached at a value of Re_τ that is only three times larger than the unstratified value of 35. As shown in figure 11, in the asymptotic regime of high Re, $Re > 4000$, intermittent dynamics appears at $L^+ \approx 200$, and the intermittency factor γ quickly drops for smaller values.

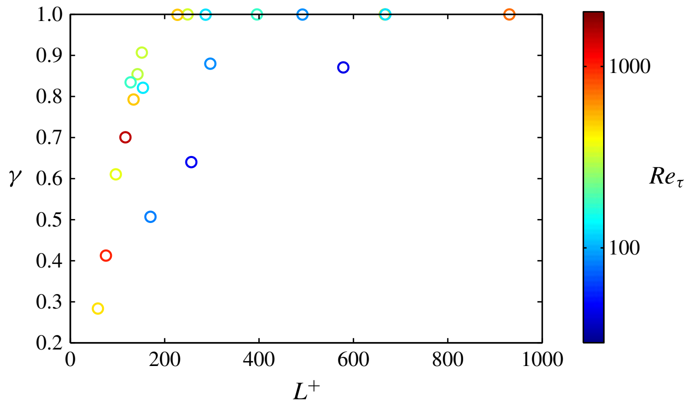

FIGURE 11. A plot of γ versus L^+ for the entire set of simulations. The colour code represents Re_τ, ranging from 40 (blue) to 1500 (red).

5. Mixing

One of the most controversial issues regarding stably stratified shear flows concerns the quantification of the irreversible mixing across isopycnals and its ratio with the energy lost to internal energy through viscosity. At least part of the problem is that there are many possible measures that can be constructed for the 'mixing efficiency' (see, for example, Salehipour & Peltier 2015). In the context of shear flow, turbulent kinetic energy is typically extracted from the mean flow by the turbulence production term,

$$P = \left\langle -\overline{u'v'} \frac{\partial \overline{u}}{\partial y} \right\rangle, \tag{5.1}$$

and undergoes a down-scale turbulent cascade until it is dissipated by viscous effects at small scales. In the presence of a stable stratification, turbulent kinetic energy can also be converted to potential energy (and vice versa) via the buoyancy flux,

$$\mathscr{B} = Ri \, \langle -\overline{v'T'} \rangle. \tag{5.2}$$

Similarly to turbulent kinetic energy, potential energy also generates a down-scale turbulence cascade, and diffusive effects convert it to background potential energy at small scales. A classical measure of the efficiency of mixing is the flux Richardson number (see, e.g., Turner 1979),

$$Ri_f(y) = \frac{Ri \, \langle -\overline{v'T'} \rangle}{\left\langle -\overline{u'v'} \dfrac{\partial \overline{u}}{\partial y} \right\rangle}, \tag{5.3}$$

representing the ratio between the buoyancy flux $\mathscr{B}$ and the turbulence production P. Figure 12 shows the $Ri_f(y)$ profiles for simulations 9, 11 and 13. The bands around the solid lines represent the standard deviation of Ri_f calculated from the time variation of Ri_f. It can be seen that $Ri_f(y)$ shows a very similar behaviour to Ri_g, with low values at the wall and a rather broad maximum at the centre, even though the values of Ri_f are slightly larger. This indicates that for the simulations considered here the turbulent Prandtl number $Pr_T = Ri/Ri_f = \nu_T/\kappa_T$ is slightly smaller than unity, where ν_T and κ_T are the eddy viscosity and the eddy diffusivity respectively. Fluctuations around mean values are significantly stronger at the centre and rapidly reduce near the walls.

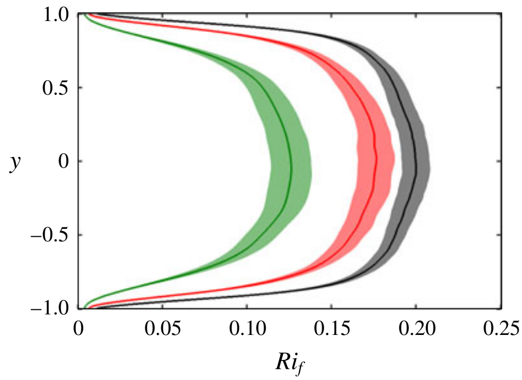

FIGURE 12. Vertical variation of $Ri_f(y)$, as defined in (5.3). The shaded regions represent the $\pm\sigma$ intervals, where σ is the standard deviation. Lines: left, simulation 9; middle, simulation 11; right, simulation 13.

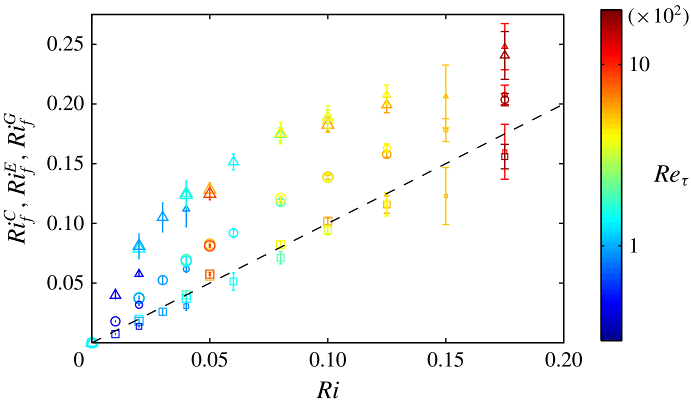

FIGURE 13. Comparison of different measures of Ri_f for the simulations listed in table 1. The symbols represent (△) Ri_f^C, derived from $Ri_f(y)$ vertically averaged in the centre $-0.1 < y < 0.1$, (○) Ri_f^E, derived from $Ri_f(y)$ averaged over the entire channel $-1 < y < 1$, and (□) Ri_f^G given by (5.9). The error bar corresponds to $\pm\sigma$, where σ represents the standard deviation of time varying quantities. The dashed black thin line represents the bisect, i.e. $Ri_f = Ri$. Data markers are colour-coded proportional to the simulation value of $\log_{10} Re_\tau$, ranging from 40 (blue) to 1500 (red), with the size of the markers proportional to the turbulent fraction γ.

Thus, $Ri_f(y)$ is a spatially varying local measure of the mixing efficiency. In figure 13, we compare two different derived measures of Ri_f. The triangles represent values of Ri_f^C, i.e. $Ri_f(y)$ averaged locally at the centre of the channel $0.1 < y < -0.1$, and the circles represent values of Ri_f^E, i.e. $Ri_f(y)$ averaged globally across the entire channel $-1 < y < +1$. Because of the lower values of Ri_f observed at the wall, Ri_f^C is larger than Ri_f^E. Nevertheless, both sets of data show a clear increase with Ri and a tendency to saturate for large values. Unfortunately, the relatively small Re did not allow us to obtain turbulent states for $Ri > 0.175$, where the behaviour of Ri_f is most debated and non-monotonic dependence in Ri is sometimes seen in experiments (see, e.g., Linden 1979; Park *et al.* 1994; Holford & Linden 1999; Oglethorpe *et al.* 2013).

The simplified wall-bounded nature of stratified PCF also allows us to identify another global measure of mixing in terms of properties of the wall forcing. By integrating the kinetic energy and the potential energy, defined as $-Ri\int Ty\,\mathrm{d}V$, over the whole domain, we can derive an evolution equation for the total energy of the system:

$$\frac{\mathrm{d}E_{TOT}}{\mathrm{d}t} = 2\tau_w - \int_{-1}^{+1} (\varepsilon_M + \varepsilon_K + \varepsilon_P)\,\mathrm{d}y, \tag{5.4}$$

where $2\tau_w$ represents the forcing due to the counter-moving walls and the ε_i terms represent the dissipation of mean kinetic energy,

$$\varepsilon_M = \frac{1}{Re}\left\langle \frac{\partial \overline{u}}{\partial x_j}\frac{\partial \overline{u}}{\partial x_j}\right\rangle, \tag{5.5}$$

turbulent kinetic energy,

$$\varepsilon_K = \frac{1}{Re}\left\langle \overline{\frac{\partial u_i'}{\partial x_j}\frac{\partial u_i'}{\partial x_j}}\right\rangle, \tag{5.6}$$

and potential energy,

$$\varepsilon_P = \frac{1}{Re\,Pr}\left\langle \overline{\frac{\partial \tilde{T}}{\partial x_j}\frac{\partial \tilde{T}}{\partial x_j}}\right\rangle, \tag{5.7}$$

where u' is the velocity fluctuation around the mean and $\tilde{T}$ is the temperature fluctuation around a linear stratification. In a statistically steady state, equation (5.4) can be reduced to the dimensionless form

$$1 - Ri_f^G = (\tilde{\varepsilon}_M + \tilde{\varepsilon}_K)\frac{Re^2}{Re_\tau^2}, \tag{5.8}$$

where $\tilde{\varepsilon}_M$ is the y-integrated mean kinetic energy dissipation and $\tilde{\varepsilon}_K$ is the integrated turbulent kinetic energy dissipation. Thus, Ri_f^G is a global measure of the mixing,

$$Ri_f^G = \frac{Ri\,Re\,(Nu-1)}{Re_\tau^2\,Pr}, \tag{5.9}$$

and we also plot this measure in figure 13 with squares. It is seen that Ri_f^G attains smaller values than Ri_f, due to the fact that Ri_f^G also includes contributions of mean kinetic energy dissipation in the denominator, which is large near the wall. This effect can be identified directly by rewriting Ri_f^G as

$$Ri_f^G = \frac{-Ri\displaystyle\int \langle\overline{v'T'}\rangle\,\mathrm{d}y}{\displaystyle\int\left\langle \frac{\partial}{\partial y}\left[\left(\frac{1}{Re}\frac{\partial\overline{u}}{\partial y} - \overline{u'v'}\right)\overline{u}\right]\right\rangle\mathrm{d}y} = \frac{-Ri\displaystyle\int \langle\overline{v'T'}\rangle\,\mathrm{d}y}{\displaystyle\int \langle\tilde{\varepsilon}_M\rangle\,\mathrm{d}y - \int\left\langle \overline{u'v'}\frac{\partial\overline{u}}{\partial y}\right\rangle\mathrm{d}y}, \tag{5.10}$$

where the fact that the total shear $\nu\partial\overline{u}/\partial y - \overline{u'v'}$ is constant has been used. Equation (5.10) indicates that reductions relative to Ri_f^C and Ri_f^E arise as a consequence of mean kinetic energy dissipation (first term in the denominator), which is large close to the walls.

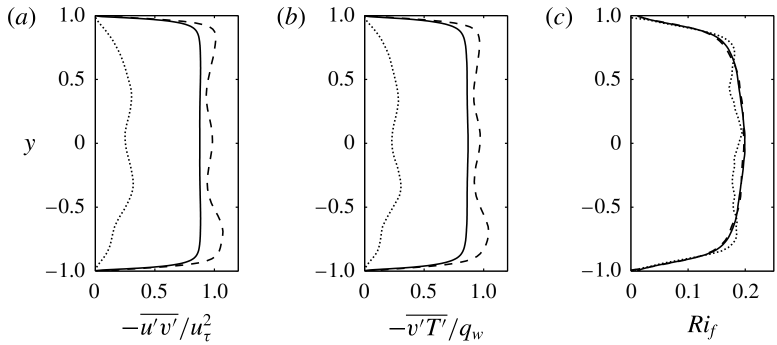

FIGURE 14. Comparison between the conditional average based on turbulent regions (- - - -) and the conditional average based on laminar regions (· · · · · ·) for simulation 13. Conditional values are obtained by averaging the horizontally averaged values over roughly 30 snapshots. The non-conditional values (——) obtained by averaging in time, i.e. $\langle\cdot\rangle$, are also shown for reference. Vertical variation of (*a*) turbulent shear stress $-\overline{u'v'}/u_\tau^2$, (*b*) turbulent heat flux $-\overline{v'T'}/q_w$ and (*c*) flux Richardson number Ri_f as defined in (5.3).

The Ri_f^G data points approximately follow a straight line corresponding to $Ri_f^G = Ri$, suggesting that velocity and temperature are closely related and show very similar behaviour such that $q_w \approx \tau_w$. This is consistent with the finding of Cenedese & Adduce (2008) and Wells, Cenedese & Caulfield (2010), who suggest a scaling of the mixing efficiency at 'weak' stratification proportional to the inverse square of an appropriate Froude number, which here is equivalent to the first power of the bulk Richardson number, $Fr^{-2} \sim Ri$. It is apparent that simulations at large Re and Ri generally show a somewhat larger degree of fluctuations of Ri_f^G. In particular, simulation 14 exhibits the largest variance, possibly due to the strong degree of intermittency found in this case. In order to investigate to what extent Ri_f depends on the global intermittency of the flow, the size of the symbols in figure 13 has been modified to reflect the value of γ. Surprisingly, the dependence of Ri_f on γ is relatively small. To understand better how laminar and turbulent regions contribute to the total mixing separately, we have calculated the turbulent shear stresses $-\overline{u'v'}$, the turbulent heat fluxes $-\overline{v'T'}$ and the flux Richardson number Ri_f in laminar and turbulent regions separately for a number of flow fields (approximately 30) of simulation 13 and averaged their values (figure 14). Fluctuations have been computed using averages applied in laminar regions and turbulent regions separately in order to avoid spurious fluctuations due to the variation of mean profiles in laminar and turbulent regions. In laminar regions, velocity and temperature fluctuations are greatly reduced with respect to their turbulent counterparts. The magnitudes of $\overline{u'v'}$ and $\overline{v'T'}$ in laminar regions drop to approximately 20–25 % of the equivalent magnitude in turbulent regions. Nevertheless, despite this reduction, Ri_f does not significantly change, indicating that $\overline{u'v'}$ and $\overline{v'T'}$ decrease proportionately such that their ratio remains close to constant. This highlights once more the close relationship between the velocity and the temperature fields. Momentum fluxes and heat fluxes both originate from the vertical advection of mean velocity and mean temperature gradients, and they reduce in the same manner as the vertical velocity fluctuation drops. This is an unexpected result as it is typically argued that more quiescent (i.e. laminar) regions should be associated with smaller mixing efficiencies since the surviving waves can still transport energy but not heat. It is important to remember that the regions that we

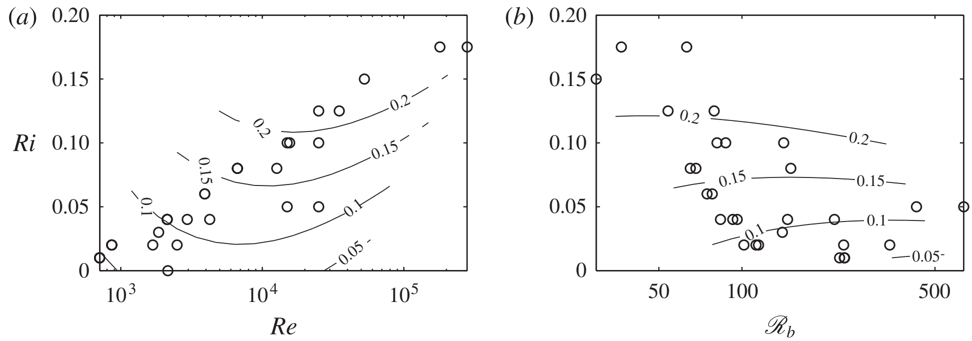

FIGURE 15. Interpolated surface of Ri_f on (*a*) an *Re*–*Ri* and (*b*) an $\mathscr{R}_b$–*Ri* plane. The symbols mark the values for the simulations in table 1.

refer to as 'laminar' are in fact constantly deformed and convected by the surrounding turbulence, still retaining 20–25 % of the turbulent fluctuations. This, together with the imposed mean velocity gradients, generates momentum and heat fluxes associated with Ri_f similar to the ones found in turbulent regions.

An understanding of how the efficiency of mixing varies as a function of *Re* and *Ri* is one of the most important problems in stratified turbulent dynamics and is certainly of central importance for parametrisation of mixing in large-scale models (see Ivey, Winters & Koseff 2008). We have attempted to unravel the shape of the $Ri_f = f(\log_{10} Re, Ri)$ surface by finding the surface that best approximates our observations. In appendix A, we outline the interpolation method in more detail. The contour levels of Ri_f, shown in figure 15(*a*), display a weak non-monotonic behaviour in *Re* with the presence of a local maximum close to the region where intermittency appears. It would be interesting to explore whether this reduction of Ri_f observed at large *Re* is real or is an artefact of the interpolation. Unfortunately, this regime is currently inaccessible due to the large computational cost associated with large Re_τ. In order to frame our results in the light of the recent advances in the understanding of stratified turbulence (e.g. Billant & Chomaz 2001; Lindborg 2006; Brethouwer *et al.* 2007), figure 15 shows the Ri_f surface in a plane where *Re* has been replaced by the buoyancy Reynolds number (Brethouwer *et al.* 2007),

$$\mathscr{R}_b = \frac{\varepsilon_K Re}{Ri}. \tag{5.11}$$

On the $\mathscr{R}_b$–*Ri* plane, the variation of Ri_f is somewhat smoothed and Ri_f is approximately constant with $\mathscr{R}_b$, with $\mathscr{R}_b$ in the range between 30 and 650. Figure 15(*b*) also shows the intrinsic limitations and difficulties of simulating stratified turbulent flows. Because of the reduction of vertical length scale due to a stable stratification, $\mathscr{R}_b$ decreases as we move towards the top right corner of figure 2(*a*), corresponding to larger values of both *Re* and *Ri*.

6. Models for predicting the intermittency boundary

The L^+ criterion (i.e. $L^+ \leqslant 200$) tested in figure 11 can be particularly useful to predict where the boundary separating intermittent and turbulent dynamics lies in the *Re*–*Ri* plane. In order to construct this prediction, we rewrite L^+ as

$$L^+ = \frac{Re_\tau^4 \, Pr}{C_\kappa \, Re^2 \, Ri \, Nu}. \tag{6.1}$$

Since throughout our simulations Pr is held fixed, modelling of the functional dependence of L^+ on the externally fixed parameters Re and Ri is equivalent to constructing models for the dependence of Re_τ and Nu on Re and Ri. In the following, we compare two such models: one simple analytical model and a more complex Reynolds-averaged Navier–Stokes (RANS) model, which potentially provides an increasing degree of accuracy at the expense of simplicity.

6.1. *Monin–Obukhov self-similarity theory*

The analytical model is derived from the self-similarity theory proposed by Obukhov (1971) and Monin & Obukhov (1954). It provides analytical expressions for velocity and temperature profiles in unstable and stable stratifications. More generally, turbulent statistical moments are assumed to depend only on the vertical momentum transfer $-\overline{u'v'}$ (at first approximation equal to the wall shear stress τ_w), the buoyancy parameter $g\alpha_V$, the height from the surface y and the turbulent heat flux $-\overline{v'T'}$ (at first approximation equal to the wall heat flux q_w). Dimensional analysis therefore leads to only one independent dimensionless group, suggesting that any statistical quantity, when properly normalised, is only a function of such a group, which could be (arbitrarily) identified by

$$\boldsymbol{\xi} = \frac{y}{L}, \tag{6.2}$$

where L is the Monin–Obukhov length scale, as defined in (2.11). In particular, the mean velocity and temperature gradients (dimensional) can therefore be written as

$$\frac{\partial u}{\partial y} = \frac{u_\tau}{C_\kappa y}\phi_m(\boldsymbol{\xi}) \quad \text{and} \quad \frac{\partial T}{\partial y} = \frac{T_\tau}{C_\kappa y}\phi_h(\boldsymbol{\xi}), \tag{6.3a,b}$$

where ϕ_m and ϕ_h are dimensionless functions, the von Kármán coefficient, C_κ, is historically included in the definitions and T_τ is the friction temperature, i.e. $T_\tau = q_w/u_\tau$. At first approximation, ϕ_m and ϕ_h are assumed to be linear functions of $\boldsymbol{\xi}$, i.e.

$$\phi_m(\boldsymbol{\xi}) = 1 + \beta\boldsymbol{\xi} \quad \text{and} \quad \phi_m(\boldsymbol{\xi}) = Pr_T + \beta\boldsymbol{\xi}, \tag{6.4a,b}$$

with Pr_T being the turbulent Prandtl number and β a dimensionless constant. Despite its simplicity, Monin–Obukhov self-similarity theory has been successfully compared with *in situ* field measurements (Businger *et al.* 1971; Kaimal *et al.* 1976) and numerical simulations (García-Villalba & del Álamo 2011; Ansorge & Mellado 2014; Deusebio *et al.* 2014). In the following we develop a model based on it. By integrating the mean gradients given by (6.3) together with definitions (6.4), we arrive at an expression for the velocity and buoyancy jumps between the upper and lower walls,

$$U = 2\frac{u_\tau}{C_\kappa}\left(\log Re_\tau + \beta\frac{h}{L} + C_\kappa C_1\right) \tag{6.5}$$

and

$$T = 2\frac{T_\tau}{C_\kappa}\left(Pr_T \log Re_\tau + \beta\frac{h}{L} + C_\kappa C_2\right), \tag{6.6}$$

with C_1 and C_2 being constants. We note that Monin–Obukhov theory assumes a very similar shape for the velocity and temperature mean profiles, consistently with our

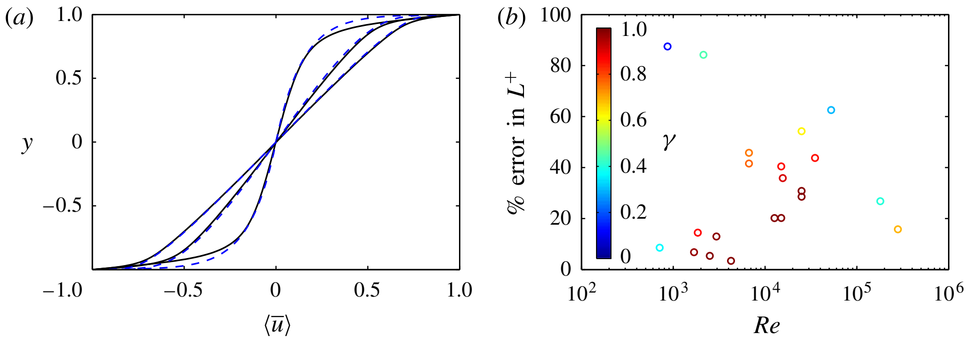

FIGURE 16. (*a*) Comparison between numerical simulations (——) and the analytical model (- - - -) defined in (6.5) and (6.6). The three profiles correspond to $\langle\overline{u}\rangle$ velocity profiles for the simulations 6, 11 and 13, shown in figure 3. (*b*) Percentage errors in the estimation of L^+ using the Monin–Obukhov model, as defined in (6.9). The symbols represent all of the simulations given in table 1 and are coloured by the turbulent fraction γ, ranging from blue (laminar) to red (fully turbulent).

simulations, as shown by the empirically observed scaling $Ri_f^G \sim Ri$. Equations (6.5) and (6.6) can be rearranged to provide expressions relating Re_τ, Re, L and Ri, i.e.

$$Re = \frac{Re_\tau}{C_\kappa}\left(\log Re_\tau + \beta\frac{Re_\tau}{L^+} + C_1\right) \tag{6.7}$$

and

$$Ri = \frac{h}{L}\,\frac{Pr_T \log Re_\tau + \beta\dfrac{Re_\tau}{L^+} + C_2}{\left(\log Re_\tau + \beta\dfrac{Re_\tau}{L^+} + C_1\right)^2}, \tag{6.8}$$

from which the value of L^+ can be estimated. Here, we set $\beta = 4.8$, $Pr_T = 0.7$ and $C_1 = C_2 = 5.5$ in (6.7) and (6.8), similar to the values suggested by Wyngaard (2010) and consistent with our simulations, indicating a Pr_T slightly smaller than unity.

Figure 16(*a*) shows a comparison between the velocity profiles from the numerical simulations (already presented in figure 3) and the predictions provided by the Monin–Obukhov theory. Despite its simplicity, we observe a reasonable agreement, particularly in the core region of the flow. On the other hand, the agreement close to the walls is less good (especially for the unstratified simulation 6 for which Re may well be too small to allow the development of a proper logarithmic layer), resulting in an error in the prediction of Re_τ and L^+. In figure 16(*b*) we plot the percentage error difference,

$$\frac{|L^+_{DNS} - L^+_M|}{L^+_{DNS}}\,\%, \tag{6.9}$$

between the value obtained from the numerical simulations, L^+_{DNS}, and the estimated value of the model using (6.7) and (6.8), L^+_M. It is worth noting that the error in the prediction of L^+ tends to be larger when intermittency appears in the flow. In fully developed turbulent regimes the predicted value of L^+ is within a relative error of 20–40 %, which we believe is acceptable.

6.2. *Explicit algebraic models*

The more complex model we consider here is an EAM for turbulent Reynolds stresses and heat fluxes for stably stratified flows. An EAM is generally developed from differential Reynolds-stress models (DRSMs) in which the evolution equations for the Reynolds stresses and heat fluxes take the form (Pope 2000)

$$\frac{\mathrm{D}\overline{u_i u_j}}{\mathrm{D}t} - \mathscr{D}_{ij} = \mathscr{P}_{ij} + \varPi_{ij} - \varepsilon_{ij} + \mathscr{G}_{ij} \tag{6.10}$$

and

$$\frac{\mathrm{D}\overline{u_i \theta}}{\mathrm{D}t} - \mathscr{D}_{\theta i} = \mathscr{P}_{\theta i} + \varPi_{\theta i} - \varepsilon_{\theta i} + \mathscr{G}_{\theta i}, \tag{6.11}$$

where the terms correspond to (from left to right) advection, diffusion, production, pressure redistributions, dissipation and buoyancy. Following Lazeroms *et al.* (2013), equations (6.10) and (6.11) can be recast as evolution equations for the dimensionless counterparts $a_{ij} = \overline{u_i u_j}/K - 2/3\delta_{ij}$ and $\xi_i = \overline{u_i\theta}/\sqrt{K K_\theta}$, where K is the turbulent kinetic energy, $\overline{u_i u_i}/2$, and K_θ is the scalar variance, $\overline{\theta^2}/2$. In EAMs, the weak-equilibrium assumption (Rodi 1976) is generally made at this stage, neglecting advection and diffusion terms in the evolution equations for a_{ij} and ξ_i. This allows one to reduce these equations to an algebraic form in which time derivatives and higher-order spatial derivatives of Reynolds stresses disappear, i.e.

$$\frac{\overline{u_i u_j}}{K}(\mathscr{P} - \varepsilon + \mathscr{G}) = \mathscr{P}_{ij} + \varPi_{ij} - \varepsilon_{ij} + \mathscr{G}_{ij} \tag{6.12}$$

and

$$\frac{\overline{u_i\theta}}{2}\left(\frac{\mathscr{P} - \varepsilon + \mathscr{G}}{K} + \frac{\mathscr{P}_\theta - \varepsilon_\theta}{K_\theta}\right) = \mathscr{P}_{i\theta} + \varPi_{i\theta} - \varepsilon_{i\theta} + \mathscr{G}_{ij}. \tag{6.13}$$

In (6.12) and (6.13), the terms $\varPi_{ij}$ and $\varPi_{i\theta} - \varepsilon_{i\theta}$ can be modelled following Launder (1975), with expressions involving K, K_θ and the other variables, i.e. U_i, T, a_{ij} and ξ_i. The dissipation term ε_{ij} is assumed to be isotropic, i.e. $\varepsilon_{ij} = (2/3)\varepsilon\delta_{ij}$, where ε is the turbulent kinetic energy dissipation. Equations (6.12) and (6.13) are implicit in a_{ij} and $\boldsymbol{\xi}$ and highly nonlinear. However, explicit algebraic equations relating a_{ij} and $\boldsymbol{\xi}$ to the other mean quantities can be derived by expanding a_{ij} and $\boldsymbol{\xi}$ in tensor groups (Pope 1975) and using an approximate equation for the kinetic energy production-to-dissipation ratio (Lazeroms *et al.* 2015). These relations together with suitable expressions for K, K_θ and ε such as the K–ω model (Menter 1992) form a closed set of equations which can be numerically solved in time. For further details on the derivation of the model we refer the interested reader to Lazeroms *et al.* (2013, 2015).

Explicit algebraic models have been successfully applied to stably stratified shear parallel flows and stably stratified channel flows, and provide fair agreement with simulations and significant improvements with respect to standard eddy-viscosity and eddy-diffusivity models (Lazeroms *et al.* 2013). In the following, we extend this comparison to PCF. It is worth emphasising here that all of the modelling constants are the same as in Lazeroms *et al.* (2013). The velocity (figure 17*a*) and density profiles (not shown) agree reasonably well with the numerical simulations over the entire channel depth. Figure 17(*b*) shows the percentage error, as defined in (6.9) using EAMs for estimating the model value L_M^+. The agreement is somewhat poor at low Re but improves for increasing Re, providing good predictions for $Re > 5 \times 10^3$. That models and simulations do not agree at low $Re < 5 \times 10^3$ is not surprising since

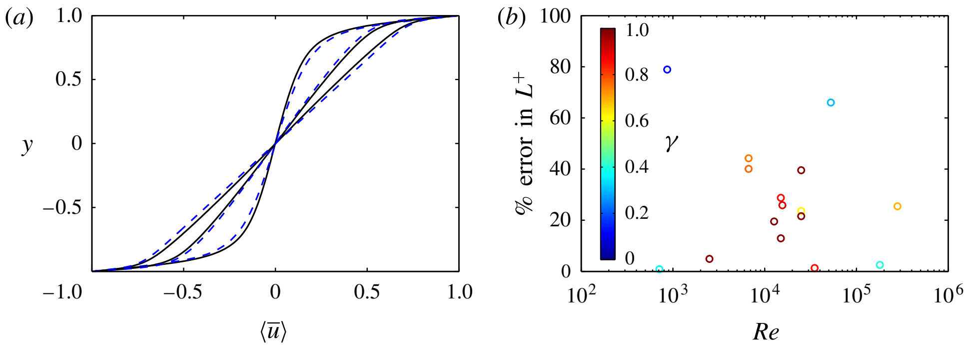

FIGURE 17. (*a*) Comparison between numerical simulations (——) and the EAM (- - - -) from Lazeroms *et al.* (2013). The three profiles correspond to $\langle \overline{u} \rangle$ for the simulations 6, 11 and 13, shown in figure 3. (*b*) Percentage errors in the estimation of L^+ using the analytical model. The symbols represent the simulations given in table 1 and are coloured by the turbulent fraction γ, ranging from blue (laminar) to red (fully turbulent).

at such low *Re* diffusive effects may well be important and the weak-equilibrium assumption may be inappropriate. Nevertheless, as long as *Re* is large enough, the relative errors for estimating Re_τ and L^+ are approximately 10 % and 20 % respectively, slightly better than for the Monin–Obukhov self-similarity theory.

6.3. *The intermittency boundary*

We now use the models outlined in §§ 6.1 and 6.2 to predict the intermittency boundary in the *Re*–*Ri* plane between turbulent and intermittent dynamics. According to figure 11, we predict that intermittency onsets at $L^+ \approx 200$. Using the two models, we have estimated L^+ as a function of *Re* and *Ri*, with *Re* between 10^3 and 10^6 and *Ri* between 0 and 0.2. A summary of the simulations together with the intermittency boundaries predicted by the two models is shown in figure 18. The colours represent the turbulent fraction γ. The two models show an overall similar behaviour, and they are indistinguishable for most of the *Re* range. Remarkably, the model based on the Monin–Obukhov self-similarity theory is able to provide good agreement with the numerical simulations and with the more complex EAM. It is nevertheless worth noting that PCF is a simple and idealised geometry in which, in statistically steady states, momentum and heat fluxes are constant across the channel. Analytical models may provide somewhat poorer performance in more complex flow geometries, where more refined models, such as EAM, have already been shown to provide better results. As shown in figure 18, at least at smaller *Re* and *Ri*, the intermittency and relaminarisation boundaries are quite close. It is still an open question whether this observation carries over to larger values of *Re* and *Ri*, particularly in sufficiently large computational domains.

7. Conclusions

We have studied the onset of global intermittency in stably stratified PCFs using numerical simulations, in an attempt to identify the intermittency boundary depicted schematically by the solid line in figure 1. We have explored the flow dynamics for a number of *Re*–*Ri* values, ranging from low *Re* ∼ 700 (close to providing intermittent dynamics in unstratified conditions) to high *Re* $\sim 2.8 \times 10^5$. The *Ri* at which intermittency arises increases with *Re*, and no turbulent states have been

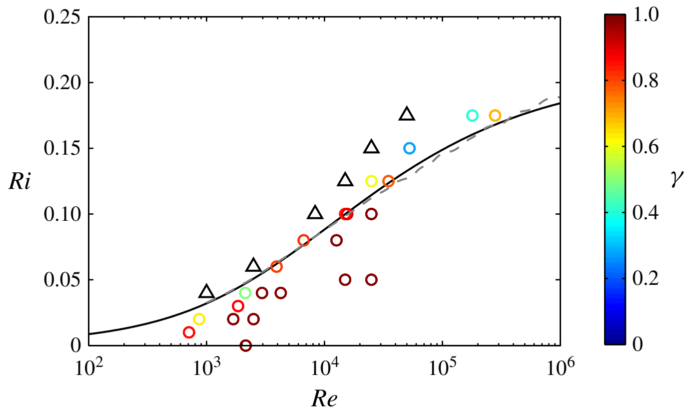

FIGURE 18. Summary of the direct numerical simulations (circles) and predictions of the intermittency boundary given by the Monin–Obukhov theory (solid black line) and the EAM (dashed grey line). The symbols are coloured by the turbulent fraction γ, ranging from blue (laminar) to red (fully turbulent). Triangles representing simulations that fully relaminarised are also shown for reference.

found for $Ri \geqslant 0.2$ for the Re considered here. At the largest Re we have considered, $Re = 2.8 \times 10^5$, a value of $Ri = 0.175$ already leads to intermittency, with a significant portion of the flow being laminar.

Intermittency first appears in the form of laminar spots which grow and decay within the flow. As Ri increases, these regions grow larger and turbulent bands span the entire domain, similar to the behaviour reported by Brethouwer *et al.* (2012). The dynamics of the laminar/turbulent patches show remarkably different features depending on Re. At low Re, viscously driven intermittency is characterised by laminar and turbulent regions which fill the entire channel gap and align horizontally along inclined bands, similar to the behaviour that has been previously reported in unstratified PCF. On the other hand, at high Re and Ri, buoyancy-driven intermittency leads to inhomogeneity in the vertical direction with an interplay of turbulent and laminar layers. At high Re, we find the layers to be homogeneous in the streamwise direction, although the size and structure of these layers might be affected and constrained by the size of the computational domain. Further investigation is needed in order to address the effect of the size of the computational domain on the laminar and turbulent structures.

The smallest turbulent fraction is generally found at the walls where the relaminarisation process of PCF is most likely to initiate. We argue that the wall dynamics in PCF is particularly important as it determines the amount of energy injected into the system and the vertical momentum flux. Based on this observation, we have developed a method for identifying laminar and turbulent regions based on local variations of wall enstrophy and we have estimated the intermittency as the fraction γ of the total wall area that is turbulent. One of our major findings is that γ depends only on L^+ when Re is sufficiently high, i.e. $Re_\tau > 100$. This value can be used to determine the onset of intermittency as suggested by Flores & Riley (2010), allowing the identification of the intermittency boundary. We find continuously statistically steady turbulent states only when $L^+ > 200$. For $L^+ < 200$, γ quickly decreases, thus suggesting $L^+ \approx 200$ as the criterion separating fully developed turbulence and intermittent flows for buoyancy-driven intermittency. Although we have not attempted to identify the relaminarisation boundary, we note that in simulations close to full relaminarisation, $L^+ \approx 60$–70. It is worth comparing these values with the results of Jiménez & Pinelli (1999), who simulated synthetic wall-bounded flows where the turbulent fluctuations in the outer flow were filtered out. This allowed them to study to what extent the near-wall cycle evolves independently and/or relies on sources/events in the outer layer. They found that the flow relaminarised (the horizontal sizes were larger but comparable to the minimal flow unit of Jiménez & Moin 1991) when the filter height $\delta^+ < 60$.

It is natural to draw a comparison between L^+ and δ^+, as L^+ is generally interpreted from a physical standpoint as the distance from the wall at which stratification becomes of leading importance. At $y^+ = L^+$, buoyancy conversion becomes comparable to shear production and substantially affects the overall energy budget. Thus, the stabilising effect of stratification damps the turbulent fluctuations for $y > L$ and buoyancy might act in an analogous manner to the filter of Jiménez & Pinelli (1999), although the stabilising effect is here provided by a physical process. Stratified flows genuinely offer the physical possibility (thus allowing experiments to be carried out) to study the interaction of outer structures and near-wall structures, and represent a powerful testbed to understand their interplay at high *Re*.

Not surprisingly, the L^+ criterion does not apply for moderately low *Re*, and marked intermittency already appears at $L^+ \approx 300$ for the set of simulations at the two lowest values of Re_τ, as listed in table 1. At such low *Re*, the onset of intermittency and ultimate relaminarisation is not buoyancy-driven but rather viscosity-driven, and the L^+ criterion alone is not expected to be relevant. Previous simulations in intermittent stably stratified Ekman layers (Deusebio *et al.* 2014) have shown laminar patches around $L^+ \approx 500$, although the *Re* considered in that study may well have been too low for the flow to be in the range of buoyancy-driven intermittency. A comparable Re_τ might be estimated using their friction velocity u_τ and the height of the low-level jet, providing a value of $Re_\tau \approx 150$, slightly larger but comparable to the threshold for buoyancy-driven intermittency $Re_\tau > 100$ that we give here. We nevertheless point out that if relaminarisation is a near-wall process involving the suppression of the near-wall cycle, we do not expect the actual value of L^+ to vary greatly depending on the flow geometry and on the exact form of the outer structures. Whether the $L^+ = 200$ value would change with *Pr* is an important question to be investigated, especially in the context of oceanic turbulence and mixing.

The identification of a particular value, $L^+ = 200$, as the criterion for partial relaminarisation also makes it possible to predict where the intermittency boundary between turbulent and intermittent regimes lies in the *Re*–*Ri* plane (the solid line in figure 1). In order to construct the intermittency boundary in the *Re*–*Ri* plane, a model able to determine the functional dependence of L^+ on *Re* and *Ri* is needed, as is clear from (6.1). We have compared two models with different degrees of accuracy and complexity, one analytical model based on the Monin–Obukhov self-similarity theory (Obukhov 1971; Monin & Obukhov 1954) and an EAM for the Reynolds-averaged Navier–Stokes equations for stably stratified flows (Lazeroms *et al.* 2013). The models are able to determine Re_τ and L^+ as functions of *Re* and *Ri* within a few tens of per cent and provide very similar predictions for the intermittency boundary. The fact that Monin–Obukhov self-similarity theory provides fair agreement with the full numerical results is consistent with the empirical observation that the velocity and temperature profiles show very similar behaviour. This is also reflected by the striking observation that the global mixing measure Ri_f^G, as defined in (5.9), scales linearly with *Ri* for flows that are mostly turbulent, and the conditional averages of the flux Richardson number in laminar and turbulent regions are quite similar.

a_0	-0.22
a_1	2.9×10^{-2}
a_2	1.9×10^{-2}
a_3	4.8×10^{-2}
a_4	3.9×10^{-2}
a_5	-2.1×10^{-3}
a_6	-9.1×10^{-3}
a_7	6.0×10^{-2}
a_8	-9.6×10^{-3}
a_9	4.4×10^{-4}

TABLE 2. Coefficients of the polynomial expansion in (A 1) used to approximate Ri_f on the Re–Ri plane.

The intermittency boundary in Re–Ri space predicted by the models becomes independent of Ri at sufficiently high Re. Therefore, it is natural to ask whether the intermittency boundary asymptotes and there exists a value of Ri for which the flow would always be intermittent, or even laminar, regardless of the value of Re. Irrespective of the answer to these questions, the fact that the intermittency boundary curve flattens in figure 18 poses a severe challenge to increasing the external density contrast between the walls to produce strongly stratified interiors with $Ri \geqslant 0.2$ in PCF, without inevitably leading to relaminarisation of an at least initially turbulent flow. Nevertheless, an intriguing possibility may be offered by a change in the density boundary conditions. In particular, if salt were used instead of temperature to stratify the flow in an experiment, the Dirichlet boundary conditions used here would be naturally replaced by homogeneous (no-flux) Neumann boundary conditions at the walls, i.e. $\partial \rho / \partial y = 0$. This would ensure an unstratified flow near the wall and the maintenance of near-wall turbulence with high momentum transfers. With large shear stresses at the wall, a large amount of power would be required to drive the system, which would in turn be dissipated by stratified turbulent dynamics. Even for large Ri, the momentum fluxes through the walls must be carried throughout the system, thus requiring efficient transport in the interior that can only be provided by highly turbulent dynamics with potentially more efficient mixing, as observed in stratified mixing layers subject to primary and inevitably transient Kelvin–Helmholtz instabilities (see, e.g., Mashayek, Caulfield & Peltier 2013).

Acknowledgements

We thank W. Lazeroms for providing the EAM and for fruitful discussions on modelling of stratified wall-bounded flows. We also thank P. Linden for valuable comments on the paper and R. Kerswell and S. Dalziel for valuable discussions. The EPSRC grant EP/K034529/1 entitled 'Mathematical Underpinnings of Stratified Turbulence' is gratefully acknowledged for supporting the research presented here.

Appendix A

In order to interpolate the data points in figure 15 we use a cubic polynomial $\mathscr{P}(\log_{10} Re, Ri)$,

$$\begin{aligned} & a_0 + a_1 \log Re + a_2 Ri + a_3 \log Re^2 + a_4 \log Re\, Ri + a_5 Ri^2 \\ & + a_6 \log Re^3 + a_7 \log Re^2\, Ri + a_8 \log Re\, Ri^2 + a_9 Ri^3, \end{aligned} \tag{A 1}$$

and find the coefficients a_j that minimise the residual,

$$\sum_{i=1}^{i=N}[\mathscr{P}(\log_{10} Re^{(i)}, Ri^{(i)}|a_j, j=0, \ldots, 9) - Ri_f^{(i)}]^2 + \sum_{j=1}^{j=9} a_j^2 \lambda, \tag{A 2}$$

where the i sum extends over all the N simulations of table 1. The coefficients a_j for $j=1, \ldots, 9$ are penalised in order to avoid a perfect fit of the data, as is a common procedure in standard regression analysis. We have tested several values of λ and used $\lambda = 0.1$ as a reasonable trade-off between a general global interpolation and a small error in the prediction of the observations. Although the method outlined here allows us to capture the general trend of Ri_f, caution should certainly be used in extrapolation away from the range of our observations. Values of the coefficients a_j are given in table 2.

REFERENCES

ANSORGE, C. & MELLADO, J. P. 2014 Global intermittency and collapsing turbulence in the stratified planetary boundary layer. *Boundary-Layer Meteorol.* **153** (1), 89–116.

ARMENIO, V. & SARKAR, S. 2002 An investigation of stably stratified turbulent channel flow using large-eddy simulation. *J. Fluid Mech.* **459**, 1–42.

BARKLEY, D. & TUCKERMAN, L. S. 2005 Computational study of turbulent laminar patterns in Couette flow. *Phys. Rev. Lett.* **94** (1), 014502.

BARKLEY, D. & TUCKERMAN, L. S. 2007 Mean flow of turbulent–laminar patterns in plane Couette flow. *J. Fluid Mech.* **576**, 109–137.

BEWLEY, T. R. 2010 Numerical renaissance: simulation, optimization, and control. Renaissance, San Diego, Calif. (Available at http://numerical-renaissance.com).

BILLANT, P. & CHOMAZ, J.-M. 2001 Self-similarity of strongly stratified inviscid flows. *Phys. Fluids* **13** (6), 1645–1651.

BRETHOUWER, G., BILLANT, P., LINDBORG, E. & CHOMAZ, J.-M. 2007 Scaling analysis and simulation of strongly stratified turbulent flows. *J. Fluid Mech.* **585**, 343–368.

BRETHOUWER, G., DUGUET, Y. & SCHLATTER, P. 2012 Turbulent–laminar coexistence in wall flows with Coriolis, buoyancy or Lorentz forces. *J. Fluid Mech.* **704**, 137–172.

BUSINGER, J., WYNGAARD, J. C., IZUMI, Y. & BRADLEY, E. F. 1971 Flux-profile relationships in the atmospheric surface layer. *J. Atmos. Sci.* **28** (2), 181–189.

CENEDESE, C. & ADDUCE, C. 2008 Mixing in a density-driven current flowing down a slope in a rotating fluid. *J. Fluid Mech.* **604**, 369–388.

CHUNG, D. & MATHEOU, G. 2012 Direct numerical simulation of stationary homogeneous stratified sheared turbulence. *J. Fluid Mech.* **696** (410), 434.

COLES, D. 1965 Transition in circular Couette flow. *J. Fluid Mech.* **21** (03), 385–425.

CORRSIN, S. & KISTLER, A. L. 1955 Free-stream boundaries of turbulent flows. *NACA Tech. Rep.* 1244.

DEUSEBIO, E., BRETHOUWER, G., SCHLATTER, P. & LINDBORG, E. 2014 A numerical study of the unstratified and stratified Ekman layer. *J. Fluid Mech.* **755**, 672–704.

DOERING, C. R. & CONSTANTIN, P. 1992 Energy dissipation in shear driven turbulence. *Phys. Rev. Lett.* **69** (11), 1648.

DUGUET, Y. & SCHLATTER, P. 2013 Oblique laminar–turbulent interfaces in plane shear flows. *Phys. Rev. Lett.* **110** (3), 034502.

DUGUET, Y., SCHLATTER, P. & HENNINGSON, D. S. 2010 Formation of turbulent patterns near the onset of transition in plane Couette flow. *J. Fluid Mech.* **650**, 119.

EAVES, T. S. & CAULFIELD, C. P. 2015 Disruption of SSP/VWI states by a stable stratification. *J. Fluid Mech.* (submitted).

FLORES, O. & JIMÉNEZ, J. 2010 Hierarchy of minimal flow units in the logarithmic layer. *Phys. Fluids* **22** (7), 071704.

FLORES, O. & RILEY, J. J. 2010 Analysis of turbulence collapse in stably stratified surface layers using direct numerical simulation. *Boundary-Layer Meteorol.* **129** (2), 241–259.

GARCÍA-VILLALBA, M. & DEL ÁLAMO, J. C. 2011 Turbulence modification by stable stratification in channel flow. *Phys. Fluids* **23** (4), 045104.

GARCÍA-VILLALBA, M., AZAGRA, E. & UHLMANN, M. 2011 A numerical study of turbulent stably-stratified plane Couette flow. In *High Performance Computing in Science and Engineering'10*, pp. 251–261. Springer.

GRACHEV, A. A., FAIRALL, C. W., PERSSON, P. O. G., ANDREAS, E. L. & GUEST, P. S. 2005 Stable boundary-layer scaling regimes: the SHEBA data. *Boundary-Layer Meteorol.* **116** (2), 201–235.

HAMILTON, J. H., KIM, J. & WALEFFE, F. 1995 Regeneration mechanisms of near-wall turbulence structures. *J. Fluid Mech.* **287**, 317–348.

HOLFORD, J. M. & LINDEN, P. F. 1999 Turbulent mixing in a stratified fluid. *Dyn. Atmos. Oceans* **30** (2), 173–198.

HOWARD, L. N. 1961 Note on a paper of John W. Miles. *J. Fluid Mech.* **10** (4), 509–512.

IVEY, G. N., WINTERS, K. B. & KOSEFF, J. R. 2008 Density stratification, turbulence, but how much mixing? *Annu. Rev. Fluid Mech.* **40** (1), 169.

JIMÉNEZ, J. & MOIN, P. 1991 The minimal flow unit in near-wall turbulence. *J. Fluid Mech.* **225**, 213–240.

JIMÉNEZ, J. & PINELLI, A. 1999 The autonomous cycle of near-wall turbulence. *J. Fluid Mech.* **389**, 335–359.

KAIMAL, J. C., WYNGAARD, J. C., HAUGEN, D. A., COTÉ, O. R., IZUMI, Y., CAUGHEY, S. J. & READINGS, C. J. 1976 Turbulence structure in the convective boundary layer. *J. Atmos. Sci.* **33** (11), 2152–2169.

KARIMPOUR, F. & VENAYAGAMOORTHY, S. K. 2015 On turbulent mixing in stably stratified wall-bounded flows. *Phys. Fluids* **27** (4), 046603.

KIM, J., MOIN, P. & MOSER, R. 1987 Turbulence statistics in fully developed channel flow at low Reynolds number. *J. Fluid Mech.* **177**, 133–166.

KONDO, J., KANECHIKA, O. & YASUDA, N. 1978 Heat and momentum transfers under strong stability in the atmospheric surface layer. *J. Atmos. Sci.* **35** (6), 1012–1021.

LAUNDER, B. E. 1975 On the effects of a gravitational field on the turbulent transport of heat and momentum. *J. Fluid Mech.* **67** (03), 569–581.

LAZEROMS, W. M. J., BRETHOUWER, G., WALLIN, S. & JOHANSSON, A. V. 2013 An explicit algebraic Reynolds-stress and scalar-flux model for stably stratified flows. *J. Fluid Mech.* **723**, 91–125.

LAZEROMS, W. M. J., BRETHOUWER, G., WALLIN, S. & JOHANSSON, A. V. 2015 Efficient treatment of the nonlinear features in algebraic Reynolds-stress and heat-flux models for stratified and convective flows. *Intl J. Heat Fluid Flow* **53** (0), 15–28.

LINDBORG, E. 2006 The energy cascade in a strongly stratified fluid. *J. Fluid Mech.* **550**, 207–242.

LINDEN, P. F. 1979 Mixing in stratified fluids. *Geophys. Astrophys. Fluid Dyn.* **13** (1), 3–23.

MAHRT, L., SUN, J., BLUMEN, W., DELANY, T. & ONCLEY, S. 1998 Nocturnal boundary-layer regimes. *Boundary-Layer Meteorol.* **88** (2), 255–278.

MASHAYEK, A., CAULFIELD, C. P. & PELTIER, W. R. 2013 Time-dependent, non-monotonic mixing in stratified turbulent shear flows: implications for oceanographic estimates of buoyancy flux. *J. Fluid Mech.* **736**, 570–593.

MENTER, F. R. 1992 Improved two-equation k–ω turbulence models for aerodynamic flows. *NASA STI/Recon Technical Report* 93, 22809.

MILES, J. W. 1961 On the stability of heterogeneous shear flows. *J. Fluid Mech.* **10** (4), 496–508.

MOIN, P. & MAHESH, K. 1998 Direct numerical simulation: a tool in turbulence research. *Annu. Rev. Fluid Mech.* **30** (1), 539–578.

MONIN, A. S. & OBUKHOV, A. M. 1954 Basic laws of turbulent mixing in the surface layer of the atmosphere. *Contrib. Geophys. Inst. Acad. Sci. USSR* **151**, 163–187.

NIEUWSTADT, F. T. M. 1984 The turbulent structure of the stable, nocturnal boundary layer. *J. Atmos. Sci.* **41** (14), 2202–2216.

NIEUWSTADT, F. T. M. 2005 Direct numerical simulation of stable channel flow at large stability. *Boundary-Layer Meteorol.* **116**, 277–299.

OBUKHOV, A. M. 1971 Turbulence in an atmosphere with a non-uniform temperature. *Boundary-Layer Meteorol.* **2** (1), 7–29.

OGLETHORPE, R. L. F., CAULFIELD, C. P. & WOODS, A. W. 2013 Spontaneous layering in stratified turbulent Taylor–Couette flow. *J. Fluid Mech.* **721**, R3.

OLVERA, D. & KERSWELL, R. R. 2014 Coherent structures in stratified plane Couette flows. In *67th Annual Meeting of the APS Division of Fluid Dynamics, Bull. Amer. Phys. Soc.* **59** (20) San Francisco, California.

ÖRLÜ, R. & SCHLATTER, P. 2011 On the fluctuating wall-shear stress in zero pressure-gradient turbulent boundary layer flows. *Phys. Fluids* **23** (2), 021704.

OSBORN, T. R. 1980 Estimates of the local rate of vertical diffusion from dissipation measurements. *J. Phys. Oceanogr.* **10** (1), 83–89.

PARK, Y. G., WHITEHEAD, J. A. & GNANADESKIAN, A. 1994 Turbulent mixing in stratified fluids: layer formation and energetics. *J. Fluid Mech.* **279**, 279–311.

PHILLIPS, O. M. 1972 Turbulence in a strongly stratified fluid – is it unstable? In *Deep-Sea Res.*, vol. 19, pp. 79–81. Elsevier.

POPE, S. B. 1975 A more general effective-viscosity hypothesis. *J. Fluid Mech.* **72** (02), 331–340.

POPE, S. B. 2000 *Turbulent Flows*. Cambridge University Press.

PRIGENT, A., GRÉGOIRE, G., CHATÉ, H., DAUCHOT, O. & VAN SAARLOOS, W. 2002 Large-scale finite-wavelength modulation within turbulent shear flows. *Phys. Rev. Lett.* **89** (1), 014501.

RODI, W. 1976 A new algebraic relation for calculating the Reynolds stresses. In *Gesellschaft Angewandte Mathematik und Mechanik Workshop, Paris, France*, vol. 56, p. 219.

RORAI, C., MININNI, P. D. & POUQUET, A. 2014 Turbulence comes in bursts in stably stratified flows. *Phys. Rev.* E **89** (4), 043002.

RUDDICK, B. R., MCDOUGALL, T. J. & TURNER, J. S. 1989 The formation of layers in a uniformly stirred density gradient. *Deep-Sea Res.* A **36** (4), 597–609.

SALEHIPOUR, H. & PELTIER, W. R. 2015 Diapycnal diffusivity, turbulent Prandtl number and mixing efficiency in Boussinesq stratified turbulence. *J. Fluid Mech.* **775**, 464–500.

SMYTH, W. D., MOUM, J. N. & CALDWELL, D. R. 2001 The efficiency of mixing in turbulent patches: inferences from direct simulations and microstructure observations. *J. Phys. Oceanogr.* **31** (8), 1969–1992.

TANG, W., CAULFIELD, C. P. & KERSWELL, R. R. 2009 A prediction for the optimal stratification for turbulent mixing. *J. Fluid Mech.* **634**, 487–497.

TAYLOR, J. R. 2008 *Numerical Simulations of the Stratified Oceanic Bottom Boundary Layer*. ProQuest.

TAYLOR, J. R. & SARKAR, S. 2007 Internal gravity waves generated by a turbulent bottom Ekman layer. *J. Fluid Mech.* **590**, 331–354.

TURNER, J. S. 1979 *Buoyancy Effects in Fluids*. Cambridge University Press.

WELLS, M., CENEDESE, C. & CAULFIELD, C. P. 2010 The relationship between flux coefficient and entrainment ratio in density currents. *J. Phys. Oceanogr.* **40** (12), 2713–2727.

VAN DE WIEL, B. J. H., MOENE, A. F. & JONKER, H. J. J. 2012 The cessation of continuous turbulence as precursor of the very stable nocturnal boundary layer. *J. Atmos. Sci.* **69** (11), 3097–3115.

VAN DE WIEL, B. J. H., RONDA, R. J., MOENE, A. F., BRUIN, H. A. R. DE. & HOLTSLAG, A. A. M. 2002 Intermittent turbulence and oscillations in the stable boundary layer over land. Part I. A bulk model. *J. Atmos. Sci.* **59** (5), 942–958.

WUNSCH, C. & FERRARI, R. 2004 Vertical mixing, energy, and the general circulation of the oceans. *Annu. Rev. Fluid Mech.* **36**, 281–314.

WYNGAARD, J. C. 2010 Turbulence in the atmosphere. In *Turbulence in the Atmosphere*, vol. 1. Cambridge University Press.

ZILITINKEVICH, S. S., ELPERIN, T., KLEEORIN, N., ROGACHEVSKII, I., ESAU, I., MAURITSEN, T. & MILES, M. W. 2008 Turbulence energetics in stably stratified geophysical flows: strong and weak mixing regimes. *Q. J. R. Meteorol. Soc.* **134** (633), 793–799.